Ozone, DNA active UV radiation and cloud changes for the near global mean and at high latitudes due to enhanced greenhouse gas concentrations

Kostas Eleftheratos[1,2], John Kapsomenakis[3], Ilias Fountoulakis[4,5], Christos S. Zerefos[2,3,6], Patrick Jöckel[7], Martin Dameris[7], Alkiviadis F. Bais[8], Germar Bernhard[9], Dimitra Kouklaki[1], Kleareti Tourpali[8], Scott Stierle[10], J. Ben Liley[11], Colette Brogniez[12], Frédérique Auriol[12], Henri Diémoz[5], Stana Simic[13], Irina Petropavlovskikh[14], Kaisa Lakkala[15,16], Kostas Douvis[3]

[1]Department of Geology and Geoenvironment, National and Kapodistrian University of Athens, Athens, Greece
[2]Center for Environmental Effects on Health, Biomedical Research Foundation of the Academy of Athens, Athens, Greece
[3]Research Centre for Atmospheric Physics and Climatology, Academy of Athens, Athens, Greece
[4]Institute for Astronomy, Astrophysics, Space Applications and Remote Sensing, National Observatory of Athens (IAASARS/NOA), Athens, Greece
[5]Aosta Valley Regional Environmental Protection Agency (ARPA), Saint-Christophe, Italy
[6]Navarino Environmental Observatory (N.E.O), Messenia, Greece
[7]Deutsches Zentrum für Luft- und Raumfahrt, Institut für Physik der Atmosphäre, Oberpfaffenhofen, Germany
[8]Department of Physics, Aristotle University of Thessaloniki, Thessaloniki, Greece
[9]Biospherical Instruments Inc., San Diego, CA 92110, USA
[10]NOAA Global Monitoring Laboratory, Boulder, CO 80305, USA
[11]National Institute of Water & Atmospheric Research (NIWA), Lauder, New Zealand
[12]Univ. Lille, CNRS, UMR 8518 - Laboratoire d'Optique Atmosphérique, F-59000 Lille, France
[13]Institute for Meteorology and Climatology, University of Natural Resources and Life Sciences, Vienna 1180, Austria
[14]Cooperative Institute for Research in Environmental Sciences, University of Colorado, Boulder, CO, USA
[15]Space and Earth Observation Centre, Finnish Meteorological Institute, Sodankylä, Finland
[16]Climate Research Programme, Finnish Meteorological Institute, Helsinki, Finland

Correspondence to: Kostas Eleftheratos (kelef@geol.uoa.gr)

Abstract. This study analyses the variability and trends of ultraviolet-B (UV-B, wavelength 280–320 nm) radiation that can cause DNA damage, which are caused by climate change due to enhanced greenhouse gas (GHG) concentrations. The analysis is based on DNA active irradiance, total ozone, total cloud cover, and surface albedo calculations with the EMAC Chemistry-Climate Model (CCM) free running simulations following the RCP-6.0 climate scenario for the period 1960–2100. The model output is evaluated with DNA active irradiance ground-based measurements, satellite SBUV (v8.7) total ozone measurements and satellite MODIS/Terra cloud cover data. The results show that the model reproduces the observed variability and change of total ozone, DNA active irradiance, and cloud cover for the period 2000-2018 quite well according to the statistical comparisons. Between 50º N–50º S, the DNA-damaging UV radiation is expected to decrease until 2050 and to increase thereafter, as it was shown previously by Eleftheratos et

al. (2020). This change is associated with decreases in the model total cloud cover and negative trends in total ozone after about 2050 due to increasing GHGs. The new study confirms the previous work by adding more stations over low and mid-latitudes (13 instead of 5 stations). In addition, we include estimates from high latitude stations with long-term measurements of UV irradiance (3 stations in the northern high latitudes and 4 stations in the southern high latitudes greater than 55°). In contrast to the predictions for 50° N–50° S, it is shown that DNA active irradiance will continue to decrease after the year 2050 over high latitudes because of upward ozone trends. At latitudes poleward of 55° N, we estimate that DNA active irradiance will decrease by $8.2 \pm 3.8\%$ from 2050 to 2100. Similarly, at latitudes poleward of 55° S, DNA active irradiance will decrease by $4.8 \pm 2.9\%$ after 2050. The results for the high latitudes refer to the summer period and not to the seasons when ozone depletion occurs, i.e., in late winter and spring. The contributions of ozone, cloud and albedo trends on the DNA active irradiance trends are estimated and discussed.

1 Introduction

The observed depletion of stratospheric ozone in the middle and high latitudes in the 1980s and the 1990s was followed by a general stabilization in the 2000s and by signs of recovery in the 2010s (Solomon et al., 2016; Weber et al., 2018; Krzyścin and Baranowski, 2019). The general behavior of ozone in the last 4 decades motivated research into the response of UV variability to ozone variability during periods with and without ozone decline. UV-B radiation is of special importance because of its effects on human health and the environment. In the short-term, the biological effects of UV-B radiation on humans include skin effects (erythema, photodermatitis) and eye effects (keratitis, conjunctivitis). Long-term effects include skin cancer, skin aging and cataracts. UV radiation can also damage the immune system and DNA (Lucas et al., 2019, Section 3.2 and references therein).

Changes in UV-B radiation and their relation to the depletion of the ozone layer in the stratosphere are being studied since the early 1990s (e.g., Blumthaler and Ambach, 1990; McKenzie, 1991; Bais and Zerefos, 1993; Bais et al., 1993). Early measurements of solar UV irradiance suggested that the long-term increase of the strongly ozone dependent wavelength of 305 nm was solely attributed to the observed stratospheric ozone decline and that it was not the result of improvements of air quality in the troposphere and changes in environmental conditions (Kerr and McElroy, 1993; Zerefos et al., 1998). Later studies based on longer atmospheric measurements looked at the effects of cloud cover, aerosols, air pollutants and surface reflectance on the long-term UV variability (e.g., Bernhard et al., 2007; den Outer et al., 2010; Kylling et al., 2010; Douglass et al., 2011). Over Canada, Europe, and Japan, it was found that the observed positive change in UV-B irradiance could not be explained solely by the observed ozone change and that a large part of the observed UV increase was attributed to tropospheric aerosol decline, the so-called brightening effect (Wild et al., 2005), since cloudiness had no significant trends (Zerefos et al., 2012). At

77 high latitudes on the other hand, it was found that the long-term variability of UV-B irradiance was not

78 affected by aerosol trends but by ozone trends (Eleftheratos et al., 2015).

79 Further efforts to understand the interactions between solar UV radiation and related geophysical variables

80 were done by Fountoulakis et al. (2018). They concluded that the long-term changes in UV-B radiation

81 vary greatly over different locations over the Northern Hemisphere, and that the main drivers of these

82 changes are changes in aerosols and total ozone. Updated analysis of total ozone and spectral UV data

83 recorded at four European stations during 1996–2017 revealed that long-term changes in UV are mainly

84 driven by changes in aerosols, cloudiness, and surface albedo, while changes in total ozone play a less

85 significant role (Fountoulakis et al., 2020b). Over higher latitudes, part of the observed changes may be

86 attributed to changes in surface reflectivity and clouds (Fountoulakis et al., 2018 and references therein).

87 Dedicated studies assessing trends of UV radiation in Antarctica provided further evidence that the UV

88 indices are now decreasing in Antarctica during summer months, but not yet during spring when the ozone

89 hole leads to large UV index variability (Bernhard and Stierle, 2020). The downward trends in UV index

90 during summer are associated with upward trends in total ozone.

91 Long-term predictions of UV radiation are governed by assumptions about the future state of the ozone

92 layer, changes in clouds, changes in tropospheric pollution, mainly aerosols, and changes in surface albedo.

93 Unpredictable volcanic eruptions, increasing emissions of GHGs, effects from growing air traffic, changes

94 in air quality and changes in the oxidizing capacity of the atmosphere induce uncertainties to long-term

95 predictions of ozone and therefore to UV radiation levels (Madronich et al., 1998). The Environmental

96 Effects Assessment Panel of the United Nations Environment Programme publishes the most recent global

97 environmental effects from the interactions between stratospheric ozone, UV radiation and climate change.

98 The Panel noted that future changes in UV radiation will be influenced by changes in seasonality and

99 extreme events due to climate change (Neale et al., 2021). Simulations of surface UV erythemal irradiance

100 by Bais et al. (2011) showed that UV irradiance will likely return to its 1980 levels by the first quarter of

101 the 21st century at northern mid and high latitudes, and 20-30 years later at southern mid- and high

102 latitudes. After reaching this level, UV will continue to decrease towards 2100 in the Northern Hemisphere

103 because of the continuing increases in total ozone due to circulation changes induced by the increasing

104 GHG concentrations, whereas it is highly uncertain whether UV will reach its 1960s levels by 2100 in the

105 Southern Hemisphere (Bais et al., 2011). However, in the Arctic, large, seasonal loss of column ozone

106 could persist for much longer that commonly appreciated. Projections of stratospheric halogen loading and

107 humidity with General Circulation Model (GCM)-based forecasts of temperature, suggested that conditions

108 favorable for large Arctic ozone loss could persist or even worsen until the end of this century, if future

109 GHG concentrations continue to steeply rise. Consequently, anthropogenic climate change has the potential

110 to partially counteract the positive effects of the Montreal Protocol in protecting the Arctic ozone layer

111 (von der Gathen et al., 2021). CCM simulations of DNA-damaging UV variability analyzed by Eleftheratos

112 et al. (2020) showed that UV irradiance will likely increase at low and mid-latitudes during the second half

of the 21st century due to decreases in cloud cover driven by climate change caused by enhanced GHG concentrations.

GHG changes can be an important driver of cloudiness changes. Norris et al. (2016) provided evidence for climate change in the satellite cloud record. They estimated fewer clouds over the mid-latitudes from 1983 to 2009 and concluded that the observed and simulated cloud change patterns are consistent with poleward retreat of mid-latitude storm tracks, expansion of subtropical dry zones, and increasing height of the highest cloud tops at all latitudes. The primary drivers for these changes were found to be the increasing GHG concentrations and a recovery from volcanic radiative cooling (Norris et al., 2016). In the same direction, Schneider et al. (2019) showed that stratocumulus clouds, some of the planet's most effective cooling systems, become unstable and break up into scattered clouds under increasing GHG concentrations. They also showed that fewer clouds will trigger additional surface warming to that from the rising CO_2 levels. Both studies provided indications that increasing GHGs can affect clouds, which in turn will affect the UV radiation reaching the Earth's surface.

In this work we investigate the UV variability and trends for the near global mean (50° N–50° S) and at high latitudes due to the expected increase of GHG concentrations in the future. We show that DNA active irradiance will continue to decrease after 2050 at high latitudes due to the prescribed evolution of greenhouse gases in contrast to regions located between 50° N and 50° S where it is shown to increase. The year 2050 was chosen as a mid-point to evaluate the trends as it divides the 21st century into two equal periods, 2000-2049 and 2050-2099, but most importantly because it was noted that for a Representative Concentration Pathway (RCP) of 6.0, the Chemistry-Climate Model Initiative (CCMI, phase 1) simulations project that global total column ozone will return to 1980 values around the middle of this century (Dhomse et al., 2018). Our study confirms the previous work by Eleftheratos et al. (2020), which focused on ozone profiles from five well-maintained lidar stations at low and mid-latitudes. Here, we add more ozone and UV stations in mid-latitudes and include estimates from high latitude stations with long-term measurements of UV radiation. The analysis aims to investigate whether the increase of DNA active radiation predicted for mid-latitudes in view of climate change, will also be observed at high latitudes. To address the issue, we use the same methodology as Eleftheratos et al. (2020), in which we compare two CCM simulations; one with increasing GHGs according to RCP-6.0 and one with fixed GHGs emissions at 1960 levels. The variability of ozone from the model simulations is evaluated against solar backscatter ultraviolet radiometer 2 (SBUV/2) satellite ozone data. The variability of DNA active irradiance from the model simulations is evaluated against ground-based DNA active radiation measurements, and the variability of simulated cloud cover is evaluated against cloud fraction data from the MODerate-resolution Imaging Spectroradiometer (MODIS)/Terra v6.1 satellite dataset.

It is important to clarify the novelty of this research and its added value with respect to the previous study by Eleftheratos et al. (2020) and to point out the main differences and similarities. This research aims at investigating how increasing GHGs in the future will influence changes in total ozone, DNA active

irradiance and cloud cover at high latitudes with respect to the near global mean (50º N–50º S). Moreover, we are aiming at estimating the fraction of the DNA active irradiance changes in the future that can be explained by ozone and cloud changes using a multiple linear regression (MLR) statistical analysis. The previous study by Eleftheratos et al. (2020) did not look at high latitudes and did not apply MLR analysis to quantify the effects on the DNA weighted UV irradiance. The previous study analyzed data from 5 stations between 50º N and 50º S, while the new study uses data from 13 stations at near global scale. Finally, this study includes analysis of averages in latitude bands, which was not done in the previous study, thus providing more complete results.

The study is organized as follows. Section 2 describes the data sources and methodology. Section 3 shows the variability and projections of DNA-damaging UV radiation at high latitude stations in comparison to mid-latitude stations, and, finally, Section 4 summarizes the main results.

2 Data sources

2.1. Ground-based data

We have analyzed DNA-weighted UV irradiance data at 20 ground-based (GB) stations listed in Table 1. Although the DNA action spectrum tends to exaggerate UV effects on humans, mammals, etc., (as it was determined with bacteria and viruses and does not take the wavelength dependence of the skin's transmission into account), it is the appropriate action spectrum for studying the detrimental biological effects of solar radiation and the effective dose of UV radiation in producing skin cancer (Setlow, 1974).

Most of the stations listed in Table 1 contribute spectral UV data to the data repository of the Network for the Detection of Atmospheric Composition Change (NDACC, www.ndacc.org) at https://www-air.larc.nasa.gov/pub/NDACC/PUBLIC/stations/ (last access 4 September 2022) (De Mazière et al., 2018) and have been reported among those possessing high-quality long term UV irradiance measurements (McKenzie et al., 2019). Sites not part of NDACC are Aosta, Athens, Sodankylä, and Thessaloniki. Data from these stations are of high-quality as well (e.g., Fountoulakis et al., 2018; Fountoulakis et al., 2020a; Kosmopoulos et al., 2021; Lakkala et al., 2008). The high quality of the spectral UV measurements is ensured by applying strict calibration and maintenance protocols.

We have calculated monthly mean irradiances from noon averages for all stations listed in Table 1 (average of measurements ± 45 minutes around local noon) and compared them with the DNA active irradiance data from an EMAC sensitivity simulation (internally named SC1SD-base-02), with specified dynamics representing the recent past (2000-2018) as a means for model evaluation. The comparisons are presented in Section 3.1 and in the Supplementary materials of this study for each station separately.

2.2. Satellite data

We have analyzed the daily solar backscatter ultraviolet radiometer 2 (SBUV/2) ozone profile and total ozone data, selected to match the UV stations' locations. The data are available from April 1970 to the present, with nearly continuous data coverage from November 1978. The satellite ozone data coverage is from backscatter ultraviolet radiometer (BUV) to solar backscatter ultraviolet radiometer 2 (SBUV-2; Bhartia et al., 2013), as follows: Nimbus-4 BUV (05/1970–04/1976), Nimbus-7 SBUV (11/1978–05/1990), NOAA-9 SBUV/2 (02/1985–01/1998), NOAA-11 SBUV/2 (01/1989–03/2001), NOAA-14 SBUV/2 (03/1995–09/2006), NOAA-16 SBUV/2 (10/2000–05/2014), NOAA-17 SBUV/2 (08/2002–03/2013), NOAA-18 SBUV/2 (07/2005–11/2012), NOAA-19 SBUV/2 (03/2009–present) and Suomi NPP OMPS (12/2011–present). We calculated daily averages by averaging the measurements from all available SBUV instruments, and then we calculated monthly means from daily averages according to Zerefos et al. (2018).

Cloud fraction monthly mean data were taken from the MODIS/Terra v6.1 dataset for the period 2000–2020. We include estimates of the variability in cloudiness around each of the ground-based monitoring stations listed in Table 1. The cloud data were taken at a spatial resolution of $3° \times 3°$ around each monitoring station. We have calculated the correlation coefficients between the de-seasonalized monthly time series of cloud fraction from MODIS/Terra and EMAC CCM for their common period (03/2000–07/2018), in order to evaluate the model simulations. The seasonal component was removed from the series by subtracting from each monthly value the 2000–2018 seasonal mean. Analytical estimates are provided in Section 3.1 and in the Supplementary materials.

2.3. EMAC Chemistry climate model (CCM) simulations

We use the same CCM simulations and methodology as described by Eleftheratos et al. (2020). The simulations come from the European Centre for Medium-Range Weather Forecasts – Hamburg (ECHAM) / Modular Earth Submodel System (MESSy) Atmospheric Chemistry (EMAC) model. The EMAC model is designed to study the chemistry and dynamics of the atmosphere (Jöckel et al., 2016). The resolution applied here is 2.8º x 2.8º in latitude and longitude, with 90 model levels reaching up to 0.01 hPa (about 80 km).

We have analyzed the EMAC RC1SD-base-10 (Jöckel et al., 2016) and SC1SD-base-02 simulation results of ozone, DNA active irradiance, and total cloud cover (in %). These simulations have been performed in a "specified dynamics" (SD) setup, i.e., nudged with ECMWF ERA-Interim reanalysis data (Dee et al., 2011) for the periods January 1979 – December 2013 (RC1SD-base-10) and January 2000 – July 2018 (SC1SD-base-02), respectively, and are therefore particularly suited for a direct comparison with observations such as ground-based and satellite measurements as presented in Section 3.1 and Appendix A. We note that the SD simulation (RC1SD-base-10, which starts in 1979) is used for the comparisons during the period of ozone depletion as SC1SD-base-02 doesn't cover that period (1980's and 1990's).

214 Two free running hind-case and projection simulations have been analyzed, both based on boundary
215 conditions following the RCP-6.0 scenario: the reference simulation RC2-base-04 (1960–2100, with
216 additional 10 years spin-up; Jöckel et al., 2016) and the sensitivity simulation SC2-fGHG-01 (1960–2100),
217 in which the GHG mixing ratios have been kept at 1960 levels (Dhomse et al., 2018). The RC2-base-04 and
218 SC2-fGHG-01 simulations were forced with sea surface temperatures (SSTs) and sea ice concentrations
219 (SICs) from the Hadley Centre Global Environment Model version 2 – Earth System (HadGEM2-ES)
220 Model (Collins et al., 2011; Martin et al., 2011). These simulations were performed for the Coupled Model
221 Intercomparison Project – Phase 5 (CMIP5) multi-model data sets in the frame of the Program for Climate
222 Model Diagnosis and Intercomparison (PCMDI). For years up to 2005, the data of the "historical"
223 simulation with HadGEM2-ES is used. Afterwards, the RCP-6.0 simulation, which is initialized with the
224 historical simulation, has been employed (Jöckel et al., 2016, and reference therein). The future solar
225 forcing used for the projections, has been prepared according to the solar forcing used in the CMIP5
226 simulation HadGEM2-ES, where the SSTs and SICs are taken from Jones et al., 2011; see also Sect. 3.3 of
227 Jöckel et al., 2016. It consists of repetitions of an idealized solar cycle which is connected to the observed
228 time series in July 2008. This has been applied consistently for all projections with prescribed SSTs (RC2-
229 base) and the same holds also for the SC-simulations. Here, we deviate from the CCMI recommendations
230 consisting of a sequence of the last four solar cycles (20–23) (see Sect. 3.4 of Jöckel et al., 2016).

231 The UV-B radiation calculated by the photolysis scheme (JVAL) (Sander et al., 2014) is weighted with the
232 DNA damage potential of Setlow (1974) with the parameterization by Brühl and Crutzen (1989). The DNA
233 damaging irradiance of the NDACC database is again based on the action spectrum by Setlow (1974) and
234 parameterized using Eq. (2) of Bernhard et al. (1997). The different parameterization of the DNA action
235 spectrum in the EMAC CCM simulations and the GB measurements will likely lead to small difference
236 between the two datasets. For example, the radiative amplification factors (RAFs) for the two
237 parameterizations may not be identical, which may lead to seasonal variations because RAFs are solar
238 zenith angle and ozone dependent. To reduce such differences, we only compared de-seasonalized data.
239 The seasonal component at each station was removed by subtracting the long-term monthly mean (2000–
240 2018) from each individual monthly value. The monthly departures were then expressed in percent of the
241 long-term monthly mean.

242 Ozone and total cloud cover data from the two RC2-base-04 and SC2-fGHG-01 free running simulations
243 for the stations listed in Table 1 have been analyzed as well and respective de-seasonalized monthly means
244 were derived. Here, the monthly data were de-seasonalized with respect to the 30-year long-term monthly
245 mean (1990–2019).

246 We note here that by a separate analysis (not shown) on total cloud cover variability and trends through the
247 21st century, using the available simulations from the CCMI-1 REF-C2 set (e.g., Eyring et al., 2013), the
248 EMAC models results fall well within the range of uncertainty, close to the ensemble average.

In all simulations analyzed here, we used prescribed aerosol distributions. The prescribed aerosol effects are separated into the aerosol surface area, representing chemical effects via heterogeneous chemistry, and the radiative properties influencing the radiation budget (Sect. 3.7 of Jöckel et al., 2016). Due to a glitch, the stratospheric volcanic aerosol was not considered correctly in the free running simulations (Sect. 3.12.1 of Jöckel et al., 2016). Therefore, the dynamical effects of large volcanic eruptions (e.g. Mt. Pinatubo 1991; El Chichón 1982) are essentially not represented in the simulations, except for the contribution to the tropospheric temperature signal induced by the prescribed SSTs. For the specified dynamics simulations, however, this has been corrected. Since the aerosol distributions have been prescribed, there is no aerosol output for these simulations that we could look at. As such, we cannot investigate the impact of future changes in aerosol loading on the UV radiation reaching the surface.

In the following sections, to assist the reader to easily follow the figure content, we change the notation of our simulations as follows:

- SC1SD-base-02: further abbreviated as HIS-SD for historical specified dynamics
- RC2-base-04: further denoted as REF for reference, and
- SC2-fGHG-01: further denoted as FIX for fixed GHGs.

2.4. Statistical methods

In Section 3.1, we evaluate the variability of DNA active irradiance from the model simulations with station measurements for a nearly 20-year period (2000–2018). The comparisons were based on regression analyses between the simulated and the observed DNA active irradiance monthly data after removing variations related to the seasonal cycle. The monthly data at each station were de-seasonalized by subtracting the long-term monthly mean (2000–2018) pertaining to the same calendar month.

We have calculated the Pearson's correlation coefficients, R, between the simulated and measured DNA active irradiance (Eq. 1) and tested them for statistical significance using the t–test formula for the correlation coefficient with n–2 degrees of freedom (Eq. 2) (von Storch and Zwiers, 1999):

$$R = \frac{\sum_{i=1}^{n}(x_i - \bar{x})(y_i - \bar{y})}{\sqrt{\sum_{i=1}^{n}(x_i - \bar{x})^2}\sqrt{\sum_{i=1}^{n}(y_i - \bar{y})^2}} \tag{1}$$

Where x refers to the measured and y to the simulated data.

$$t = R\sqrt{\frac{n-2}{1-R^2}} \tag{2}$$

275 The same procedure was followed for the comparisons between the simulated and satellite derived total
276 ozone and cloud cover datasets for the period 2000–2018, which are presented in Section 3.1.

277 In Section 3.3, we apply a statistical test to compare the regression slopes in DNA active irradiances before
278 and after the year 2050. The null hypothesis, that the two slopes are statistically equal (H_0: $b_1 = b_2$), is
279 tested against the alternative hypothesis that the two slopes are not statistically equal (H_1: $b_1 \neq b_2$). The
280 difference in slopes is tested with the statistic:

$$t = \frac{b_1 - b_2}{S_{(b_1-b_2)}} = \frac{b_1 - b_2}{\sqrt{s_{b_1}^2 + s_{b_2}^2}} \tag{3}$$

281 With $n_1 + n_2 - 4$ degrees of freedom, according to Eq. (11.20) of Armitage et al. (2002). The parameter
282 $S_{(b_1-b_2)}$ is the standard error of ($b_1 - b_2$). The parameters b_1 and b_2 are the slopes before and after 2050
283 in each geographical zone, and n_1 and n_2 are the numbers of data before and after 2050, respectively. The
284 test was performed using de-seasonalized monthly values but also with the averages shown in Figures 4c,
285 5c, 6c, calculated from de-seasonalized data. Both gave similar statistical results. In Section 3.3 we present
286 the results using the de-seasonalized monthly values.

287 The slope of the regression line, where x is the time variable and y is the DNA active irradiance, is given
288 by:

$$b = \frac{\sum(x - \bar{x})(y - \bar{y})}{\sum(x - \bar{x})^2} \tag{4}$$

289 The residual mean square for the first group (1960-2049), $s_{b_1}^2$, is given by:

$$s_{b_1}^2 = \frac{\sum_{(1)}(y - Y_1)^2}{n_1 - 2} = \frac{S_{yy1} - S_{xy1}^2/S_{xx1}}{n_1 - 2} \tag{5}$$

290 And the corresponding mean square for the second group (2050-2099), $s_{b_2}^2$, by:

$$s_{b_2}^2 = \frac{\sum_{(2)}(y - Y_2)^2}{n_2 - 2} = \frac{S_{yy2} - S_{xy2}^2/S_{xx2}}{n_2 - 2} \tag{6}$$

291 Here, S_{yy} is the standard deviation of DNA active irradiance, S_{xx} is the standard deviation of time and
292 S_{xy} is their covariance, for the first (1960-2049) and second (2050-2099) periods, respectively.

293 If $|t| > t_{critical\,(n_1+n_2-4)}$, then the null hypothesis, H_0, (the slopes are equal) is rejected at the significance
294 level a, and the alternative hypothesis (the two slopes are statistically different) is accepted.

295

3 Results and discussion

3.1 Evaluation of EMAC CCM simulations for the present

The time series of de-seasonalized DNA active irradiance data are presented in Figure 1. The figure compares model calculations of DNA active irradiance from the HIS-SD simulation with ground-based measurements at stations described in Section 2. The upper panel refers to the average of de-seasonalized data at three stations in the northern high latitudes, the middle panel refers to the respective average of thirteen stations between 50° N and 50° S, and the lower panel to the respective average of four stations in the southern high latitudes. The comparisons refer to the period 2000–2018. We note that this is a composite dataset, obtained with the same set of stations (both in the model and in the observations). All timeseries in the model start from at same year, but not in the observations.

The analysis shows that the correlations between the simulated and ground-based DNA active irradiance data are statistically significant. Figure 1, however, shows that the variability between the simulated and ground-based data can be different. This becomes evident from Figure 2 which presents the respective scatter plots. We have added the linear regression line and the y=x line which shows how much the slope of the fit deviates from the 1:1 line. The statistical results (correlation coefficient, slope, error, t-value, p-value, and root mean square error (RMSE)) are summarized in Table 2a.

For the near-global mean, the correlation coefficient between the simulated and observed DNA active irradiances is +0.709, the slope of the fit is 0.521, its error is 0.035, and the RMSE is 4.423. For the northern high latitudes, the statistical results are R = 0.518, slope = 0.657, error of slope = 0.129, RMSE = 9.543, while for the southern high latitudes are R = 0.746, slope = 0.879, error of slope = 0.070, RMSE = 14.766. It appears that the slope of the regression fit for the near-global mean is small; however, the RMSE, which is the measure of the differences between the simulated and observed values, is also small. A RMSE of 0 would indicate a perfect fit to the data, something that is never achieved in practice. It also appears that the respective RMSE of the residuals (i.e., the simulated minus observed values) are larger at high latitudes; this is because it was derived from larger differences of de-seasonalized data at the northern high latitudes and even larger at the southern high latitudes.

The regression analysis results between the two data sets at each station separately are presented in the Supplement, Table S1. We note here that the model has a resolution of 2.8° x 2.8°, which is a large area to be represented by point measurements. As such, for stations with inhomogeneous surrounding area, such as mountain tops (Mauna Loa, Sonnblick, Zugspitze), valleys (Aosta), or in towns with very heterogeneous surroundings (sea, mountains) and atmospheric conditions (tropospheric ozone and aerosols), like Athens, the model simulations of DNA active irradiance are not expected to fully agree with the measurements. Thus at some stations, the correlation between simulated and measured DNA weighted UV irradiance is not

very good, as shown in the Supplement figures. For the same reason, the slope between the two datasets can deviate significantly from unity (see Supplement Table S1). Therefore, the comparisons at the individual stations provide a qualitative evaluation of the model's variability, but cannot be considered as a strict validation of the model. We provide here indicative estimates for individual stations, which give very good to excellent correlations: a) Summit, Greenland: R = +0.709, slope = 0.757, error of slope = 0.081, p-value <0.0001, N = 88, b) Hoher Sonnblick, Austria: R = +0.673, slope = 0.946, error of slope = 0.075, p-value <0.0001, N = 192, c) Boulder, CO, USA: R = +0.748, slope = 0.677, error of slope = 0.047, p-value <0.0001, N = 163, d) Arrival Heights, Antarctica: R = +0.939, slope = 1.000, error of slope = 0.033, p-value <0.0001, N = 126.

The same procedure was followed to evaluate simulated ozone and cloud cover. Figure 3 shows (a) ozone calculations from the HIS-SD simulation compared to satellite SBUV retrievals and (b) shows simulated cloud cover compared to cloud cover from MODIS/Terra. It appears that the variability of ozone from the model simulation follows exceptionally well the variability of ozone from the satellite retrievals. It also appears that the variability of cloud cover from the model simulation is quite well correlated with the variability from the satellite observations (see Tables 2b and 2c). The respective comparisons using zonally averaged data for the northern high latitudes ($55^\circ - 75^\circ$ N), the near global mean (50° N – 50° S) and the southern high latitudes ($55^\circ - 75^\circ$ S) are presented in Supplement Figure S1. The regression results (R, slope, error of slope, t-value, p-value, and RMSE) for the large-scale latitudinal averages are presented in Supplement Table S2 and they are in line with the results from the station averages.

The Supplement Table S3 presents analytically the comparisons of total ozone between the EMAC CCM calculations and SBUV satellite retrievals. The correlations between the two different data sets are statistically significant at confidence level greater than 99.9% at all stations under study. The correlation results for four indicative stations are: a) Summit, Greenland: R = +0.927, slope = 0.791, error of slope = 0.028, p-value <0.0001, N = 131, b) Hoher Sonnblick, Austria: R = +0.902, slope = 0.803, error of slope = 0.026, p-value <0.0001, N = 223, c) Boulder, CO, USA: R = +0.854, slope = 0.757, error of slope = 0.031, p-value <0.0001, N = 223, d) Arrival Heights, Antarctica: R = +0.896, slope = 0.655, error of slope = 0.029, p-value <0.0001, N = 128.

The Supplement Table S4 presents the respective comparisons for cloud cover. The cloud observations come from MODIS/Terra. The correlation results for these four stations are: a) Summit, Greenland: R= +0.196, slope = 0.069, error of slope = 0.031, p-value = 0.025, N = 131, b) Hoher Sonnblick, Austria: R = +0.556, slope = 0.619, error of slope = 0.062, p-value <0.0001, N = 222, c) Boulder, CO, USA: R = +0.539, slope = 0.482, error of slope = 0.051, p-value <0.0001, N = 222, d) Arrival Heights, Antarctica: R = +0.537, slope = 0.949, error of slope = 0.133, p-value <0.0001, N = 129.

3.2 Future changes in ozone and DNA active irradiance

In the previous section we evaluated the SD simulation SC1SD-base-02 with satellite and ground-based measurements. In this section we use the EMAC CCM simulations to investigate the evolution of DNA active irradiance and the parameters that affect its long-term variability into the future. More specifically, we have analyzed the free-running simulation of the EMAC CCM, namely RC2-base-04, with increasing GHGs according to RCP-6.0 at the stations under study. An evaluation of the free running simulation RC2-base-04 with the SD simulation SC1SD-base-02 is provided in Appendix A. It helps to evaluate the quality of the results of the free running model system with respect to the SD simulation and the observations of the stations, and it serves as a "bridge" from the observations via the SD simulation results to the results of the (longer-term) free-running model simulation.

We followed the same methodology as Eleftheratos et al. (2020), to examine the effect of increasing GHGs on the evolution of DNA active radiation. We have compared the free-running simulation RC2-base-04 with the sensitivity simulation SC2-fGHG-01 where GHGs are kept constant at 1960 levels (see also Appendix A). The difference between the two free-running simulations gives us an estimate of the desired result.

We have prepared a series of figures to demonstrate the two different simulations and the differences between them. Figure 4 is based on 13 UV stations between 50° north and south. Figure 5 shows the results for the northern high latitude stations and Figure 6 for the southern high latitude stations. The top panel refers to the evolution of total ozone anomalies from 1960 to 2100; the middle panel refers to the evolution of DNA active irradiance and the lower panel to the evolution of clouds for the same period. The left panel shows the two simulations, i.e., the free-running simulation with increasing GHGs (REF) versus the same simulation with fixed GHGs at 1960 levels (FIX) and the right panel shows their respective differences. Shown are annual averages calculated from monthly de-seasonalized data. The calculation of annual averages was done as follows: First, we de-seasonalized the monthly data at each station by subtracting the long-term monthly mean (1990–2019) pertaining to the same calendar month. Next, we calculated a monthly de-seasonalized time series for each geographical zone by averaging the monthly de-seasonalized data of the stations belonging to each geographical zone. The latter time series was used to estimate the annual data anomalies. For the northern high latitude stations, the annual average refers to the average of monthly anomalies from March to September, and for the southern high latitude stations, it refers to the average of monthly anomalies from September to March. For the stations between 50° N–50° S we used all months to calculate the annual average.

In addition, we have added with green squares the DNA-weighted UV irradiance anomalies averaged at the ground-based stations under study around local noon. We also include the total ozone anomalies from SBUV with blue dots and the respective cloud cover anomalies from MODIS/Terra (magenta triangles) averaged at the stations studied. The observational data have been added to show simply that the dispersion of the simulated data matches the dispersion of the measured data.

398   In the study by Eleftheratos et al. (2020) data from 5 stations between 50 degrees north and south were

399   analyzed. Here, we examine for this latitude band 13 stations instead of 5 (Figure 4). The new findings

400   paint the same picture: an increasing trend in DNA active irradiance after the year 2050, associated with a

401   decreasing trend in cloud cover due to the evolution of GHGs and a negative trend in total ozone (Figure

402   4c). Thus, our new results, based on 13 instead of 5 stations, confirm qualitatively the results of the

403   previous study for 50º N–50º S. An offset between total ozone from SBUV and the free running simulation

404   is evident in the 1980s, which is larger at 50º N–50º S. This is discussed later.

405   The focus now is at higher latitudes, which show a different picture than that of 50º N–50º S after the year

406   2050. At the northern high latitude stations (Figure 5), DNA active irradiance (during the summer half

407   year) shows a decreasing trend after 2050, total ozone shows an increasing trend after 2050 and cloud cover

408   does not show any obvious statistically significant trend. The estimated trends (in % per decade) and their

409   standard errors are presented in Table 3. More specifically, we estimate that total ozone will increase by 1.8

410    $\pm$ 0.8% from 2050 to 2100 (t-value = 2.169, p-value = 0.035), DNA active irradiance will decrease by 8.2 $\pm$

411   3.8% (t-value = $-$2.161, p-value = 0.036), and cloud cover will slightly increase by 1.4 $\pm$ 1.3% (t-value =

412   1.061, p-value = 0.294). Accordingly, at the southern high latitude stations (Figure 6), total ozone is

413   estimated to increase by 4.2 $\pm$ 2.1% from 2050 to 2100 (t-value = 2.020, p-value = 0.049), DNA active

414   irradiance is estimated to decrease by 4.8 $\pm$ 2.9% (t-value = $-$1.660, p-value = 0.103), and cloud cover will

415   decrease insignificantly by 1.1 $\pm$ 1.7% (t-value = $-$0.604, p-value = 0.548).

416   The above estimates point to an increase in total ozone in the northern high latitudes by the end of the

417   century on an almost year-round basis. In a recent study by von der Gathen et al. (2021), it was concluded

418   that conditions favorable for large Arctic ozone loss during cold winters could persist or even worsen until

419   the end of this century, if future abundances of GHGs continue to rise. As such, anthropogenic climate

420   change has the potential to partially counteract the positive effects of the Montreal Protocol in protecting

421   the Arctic ozone layer (von der Gathen et al., 2021). We examined the EMAC CCM projections regarding

422   this finding. We have analyzed the REF and FIX simulation results of ozone, DNA active irradiance, and

423   cloud cover for January, February, and March for the three northern high latitude stations, Summit, Barrow

424   and Sodankylä. The trend results are presented in Table 4, which shows the trends from the two

425   simulations, and their differences, for the periods 1960–1999, 2000–2049 and 2050–2099.

426   It appears that in January and February, considered as the two coldest months of the year, the trends

427   decrease from the first (2000–2049) to the second period (2050–2099), while in March (less cold month)

428   the picture is different. More specifically, in January, the significant positive trend of 1.53 $\pm$ 0.64% per

429   decade in 2000–2049 changes to 0.21 $\pm$ 0.73% per decade in 2050–2099. In February, the significant

430   positive trend of 1.79 $\pm$ 0.78% per decade in 2000–2049 decreases to 0.58 $\pm$ 0.71% per decade in 2050–

431   2099. On the other hand, the trends in March are 0.17 $\pm$ 0.58% per decade in 2000–2049 and 1.20 $\pm$ 0.51%

432   per decade in 2050–2099, and they agree with the general course of trends seen in Figure 5. We end up to

433   findings that are qualitatively in agreement with those concluded by von der Gathen et al. (2021) about the

434 large seasonal losses of Arctic ozone during cold winters until the end of the century. We also attempted to

435 estimate the trends in DNA active irradiance in the northern high latitude stations for January, February,

436 and March. The results are presented in Table 4 for the two periods, 2000–2049 and 2050–2099, but due to

437 the polar night at the northern high latitudes, UV values are very low in January and February, and the

438 predicted trends have large standard errors. As such, they are not analyzed any further.

439 Another issue is that Figure 5a suggests that clouds will stay more or less constant over the Arctic. Other

440 models predict that cloud cover in the Arctic will increase until the end of the century. With sea ice

441 diminishing in the Arctic, evaporation would increase, leading to more moisture in the air, resulting in more

442 clouds, which in turn is expected to reduce UV radiation. For example, Fountoulakis and Bais (2015)

443 analyzed changes in UV radiation projected for the Arctic. Comparison of Figure 1 (clear-sky trends) and

444 Figure 2 (all-sky trends) of Fountoulakis and Bais (2015) suggests that UV changes between the future and

445 the present will become more negative when clouds are also considered due to the projected increase in

446 cloud attenuation. Our estimates indicate a significant cloud increase of ~2.2% from 1960 to 2100 (~1.4%

447 from 2050 to 2100, not significant). These increases are small and are based on the average of three stations

448 only, Summit, Barrow and Sodankylä, but they are in accordance with the results obtained for the whole

449 latitudinal band of 55º–75º N (~2.7% from 1960 to 2100, p-value < 0.0001, and ~0.9% from 2050 to 2100,

450 p-value = 0.05). Summit and Sodankylä are far away from the seashore and are not affected by the ocean,

451 while Barrow is located only 250 m away from the coast and is greatly affected by the ocean. Changes in

452 cloudiness might be different at coastal and mainland sites. For Barrow (coastal site) we estimate a

453 significant cloud increase of 5.5% in the period 1960–2100 (3% in the period 2050–2099), while for

454 Summit (pure land site) we estimate an insignificant change of –0.1% in the period 1960–2100 (–0.4% in

455 the period 2050–2100). For Sodankylä (also pure land site), we estimate an insignificant increase of 1.2%

456 in the period 1960–2100 (p-value = 0.365), and of 1.6% in the period 2050–2100 (p-value = 0.446).

457 Averaging large and small changes in cloudiness should finally result to moderate changes. These results

458 generally agree with the results presented in other studies (Bais et al., 2015; Fountoulakis and Bais, 2015)

459 for land areas of the Arctic (keeping also in mind that the results of the present study are averages for three

460 stations only). We note that the results presented in these two referenced studies were for RCPs 4.5 and 8.5,

461 and thus not directly comparable with the results of our study. In a more recent study presenting RCP 6.0-

462 based projections (Bais et al., 2019), it was shown that cloudiness changes at high latitudes would strongly

463 affect the UV irradiance mainly over the ocean where the absence of sea ice would result to increased

464 evaporation. For land, smaller and non-significant changes were reported (see Figure 8 of Bais et al., 2019),

465 which is again in agreement with the results presented in our study. In another study (Figure 5 of

466 Fountoulakis et al., 2014), changes in zonally averaged UV irradiance due to changes in cloudiness in

467 1950–2100 were estimated to be the order of 5–15% (depending on the RCP) for latitudes ~70 degrees.

468 However, only changes over the ocean were considered in that study and not over land. Additional

469 indications that our results should be considered representative of the three stations under study and not the

470 entire Arctic region is provided in Figure B1 (Appendix B), which shows the changes in zonal mean cloud

471   cover for the Arctic region from the REF simulation. It appears that the zonal mean cloudiness is expected

472   to increase more and more as move northward of 50° towards the North pole, indicating that the largest

473   changes in cloud cover are likely to occur over the ocean and not over land.

474   For the period 1960–1999, the DNA active irradiance (summer half year) showed upward trends in all

475   geographical zones following the downward trends of total ozone. Nevertheless, we should note that the

476   examined simulation REF (simulation with full chemistry and increasing GHGs according to RCP-6.0)

477   seems to clearly underestimate the observed ozone depletion of the 1980s and 1990s in the geographical

478   region 50° N–50° S (Figure 4), but in the higher latitude regions (Figs. 5 and 6) the picture looks much

479   better. This suggests that there may be a bias in the model, that might at least partly be caused by not

480   considering all ozone depleting substances (ODSs), but only a subset (only CFC-11 and CFC-12 are

481   considered; Jöckel et al., 2016). The REF simulation also underestimates the ozone depletion of the 1980s

482   and 1990s in the northern high latitude stations (Figure 5), but the picture is better than that of 50° N–50° S.

483   The FIX simulation seems to reproduce better the Arctic ozone depletion of the past. The latter, however, is

484   coincidence; it only indicates that due to the higher dynamic variability of the northern (winter)

485   stratosphere, the evolution of the ozone layer in the Arctic region is significantly affected by natural

486   variability of the stratosphere due to planetary waves. The best agreement between the REF simulation and

487   satellite measurements during the period of ozone depletion is found for the southern high latitudes, as can

488   be seen from Figure 6. As such, we can infer that the model simulations reproduce very well the observed

489   ozone depletion of the past in particular in the southern higher latitudes, and less well in the northern higher

490   latitudes. Nevertheless, the simulated decline of ozone during 1979–1999 and the minimum ozone values

491   calculated by the model in the 1990s for the near global mean (50° N-50° S) and for the higher latitudes,

492   are qualitatively in line with the satellite ozone observations, which is a good outcome. This is supported by

493   Figure A1 (Appendix A), which shows the free running simulation REF against the SD simulation HIS-SD

494   which starts in 2000. Because we wanted to evaluate the free running simulation for the period of ozone

495   depletion, we also analyzed the SD simulation RC1SD-base-10 which starts in 1979. It appears that the

496   REF simulation seems to reproduce well the negative ozone trends during the period of ozone depletion,

497   but not the exact anomalies of a particular year. This is because the free running simulation has its own

498   meteorological/synoptical sequence, and thus we cannot expect that the observed time series of the past is

499   reproduced on a year-by-year basis in the free running simulation the same way is reproduced in the

500   simulation with "specified dynamics".

501   Finally, we should also refer to the recent assessment of the United Nations Environment Programme

502   (UNEP) Environmental Assessment Panel (EEAP) (Bernhard et al., 2020), which compared projections of

503   future UV radiation from two studies, Bais et al. (2019) and Lamy et al. (2019). We have compared our

504   trend estimates, which are based on one model only, with the estimates provided in Table 1 of Bernhard et

505   al. (2020), which are based on many models of the first phase of the Chemistry-Climate Model Initiative

506   (CCMI-1) and should therefore be considered more robust than the estimates provided here. We clarify that

507   it is only a qualitative comparison as our trends are based on DNA weighted irradiance while the table in

508 Bernhard et al. (2020) refers to erythema. The DNA radiation amplification factor is about 2.1 while that
509 for erythema is 1.2, which suggests that we would expect differences in trends by roughly a factor of 1.75.
510 We also note that the table of Bernhard et al. (2020) shows zonal mean changes of the clear-sky UV index,
511 whereas we estimate changes in DNA active irradiance based on station averages. Despite the
512 inconsistencies in the radiation fields being compared, our trend estimates from the REF simulation based
513 on RCP-6.0 are qualitatively in line with the results presented by Bernhard et al. (2020) for the case of
514 RPC-6.0. We estimate a statistically significant decrease in DNA active irradiance at the northern high
515 latitude stations for the period 2015 to 2090 of about –17% (–16% for the zonal mean 55º–75º N). The
516 numbers from Table 1 of Bernhard et al. (2020) for the northern high latitudes are –6% for the annual mean
517 clear-sky UV index for the period 2015 to 2090, and –3%, –7%, –5% and –4% for January, April, July, and
518 October, respectively. Our respective estimate for the southern high latitude stations is about –24% (–26%
519 for the zonal mean 55º–75º S) and is also qualitatively in line with the negative trend estimates provided by
520 Bernhard et al. (2020) for the southern high latitudes for the period 2015 to 2090 (–18% for the annual
521 mean clear-sky UV index, and –8%, –6%, –6% and –23% for January, April, July, and October,
522 respectively).

523 The above estimates are based on station averages. We have complemented the analysis presented in
524 Figures 4, 5, 6 with zonally averaged data in order to exploit the model results over the entire domain, for
525 example in latitudinal bands, and not only to 20 locations. The Supplement Figures S2, S3, S4 show the
526 changes from the free running simulations REF, FIX, and their differences, for the near global mean, and
527 the northern and southern high latitudes based on latitudinal averages. It appears that the results from the
528 analysis of averaging the model data in latitudinal bands are in the same direction with those of the station
529 averages. More specifically, for the near global mean we find similar results to those presented in Figure 4
530 for the stations mean, but a stronger negative trend in total ozone after 2050 which together with the
531 negative cloud trend drive the positive DNA active irradiance trend after 2050. On the other hand, negative
532 trends in total ozone and clouds after 2050 are not observed in the northern or the southern high latitude
533 belt.

534 We believe that the negative trends seen in the near-global mean after 2050 result from the ongoing
535 increases in GHGs that will affect total ozone and clouds. It is well known that increasing GHG
536 concentrations have led to tropospheric warming and stratospheric cooling over the last decades (Stocker et
537 al., 2013; Zerefos et al., 2014). As a thermodynamic consequence, the troposphere has expanded and the
538 height of the tropopause has increased (Santer et al., 2003). A recent study showed that the stratospheric
539 layer has contracted substantially over the last decades due to increasing GHGs and will continue to
540 contract under the RCP-6.0 scenario (Pisoft et al., 2021). Also, chemistry-climate and climate model
541 projections show an acceleration of the Brewer-Dobson circulation in response to GHG increases
542 (Butchard, 2014). These changes will not leave the ozone layer unaffected. Our model simulations for the
543 near-global mean show a downward trend in total ozone after 2050, which will likely be shaped by the
544 negative trend in the lower stratosphere due to increasing GHGs. For clouds, it has been shown that

545   increasing GHGs are responsible for less clouds over the mid-latitudes (Norris et al., 2016) and for

546   breaking up stratocumulus clouds into scattered clouds (Schneider et al., 2019). Our simulations show that

547   clouds will decrease in response to increasing GHGs, which is consistent with the findings of these studies.

548   The results based on the zonally averaged data fully support the basic finding of the paper that DNA active

549   irradiance is expected to change differently at high latitudes than at near-global scale after around 2050. It

550   will continue to decline at high latitudes mainly due to stratospheric ozone recovery from the reduction of

551   ODSs (cloud cover changes are not significant), while it is expected to increase on a near-global scale,

552   affected by GHG-induced reductions in cloud cover and total ozone. This of course is an outcome that

553   emerges from the simulations of a single climate-chemistry model, and as such, it may well turn out to be

554   true or false. Verification of the results from other model simulations would be important, but also

555   important is further investigation of the cloud changes from the model simulations and their verification

556   with high quality measurements. It is important to note that our free running simulations were designed

557   according to the definitions for the reference and sensitivity simulations provided by the IGAC and SPARC

558   communities to address emerging science questions, improve process understanding and support upcoming

559   ozone and climate assessments (Eyring et al., 2013).

560

561   3.3 Statistical evaluation of differences between trends and statistical modelling

562   We have compared the regression slopes in DNA active irradiances before and after the year 2050.

563   Our calculations according to Eq. 3 show that at the significance level $\alpha = 0.05$, the null hypothesis that the

564   slopes are statistically equal, cannot be rejected for neither the northern, nor the southern high latitudes

565   (>55º), and therefore we cannot conclude that there is any statistically significant difference between the

566   trends in DNA active irradiance before and after 2050 in these two latitude zones. On the other hand, the

567   null hypothesis is rejected for the latitude zone of 50º N–50º S, which means that the alternative hypothesis

568   is accepted, and so the two trends before and after 2050 are statistically different. The statistical results are

569   presented in Table 5.

570   We note here that the statistical test was also applied for the periods before 2050, i.e., the two periods 1960-

571   1999 and 2000-2049, to test if their trends are statistically significant or not. In all latitudes it was found

572   that the regression slope of the period 1960-1999 is not statistically significantly different from the

573   regression slope of the period 2000-2049. As such, it appears that only after the year 2050 there appears to

574   be a statistically significant change in the trends of DNA active irradiance because of the evolution of

575   GHGs and only at latitudes between 50º N and 50º S. At latitudes poleward of 55º, the DNA active

576   irradiance is more likely to continue to decrease due to the increasing ozone trends from the reduction of

577   the concentrations of ODSs.

578   Moreover, we have applied multiple linear regression (MLR) analysis to examine the contribution of ozone

579   and cloud trends to the estimated DNA active irradiance trends after the year 2050. The MLR model was

580 applied to the differences between the two model simulations, REF and FIX, which were estimated from
581 monthly de-seasonalized data (*deseas*). The MLR model is of the following form:

$$deseas\ DNA\ active\ irradiance = a + \beta_{O_3} \cdot deseas\ O_3 + \beta_{cloud} \cdot deseas\ Cloud \quad (7)$$

582 Where, a is the intercept, β_{O_3} is the ozone coefficient and β_{cloud} is the cloud coefficient for the period
583 2050–2099. The regression coefficients and their standard errors are presented in Table 6a. These
584 coefficients were derived from station mean data, and hence might not be representative for the entire
585 geographical zones. As can be seen, the coefficients β_{O_3} and β_{cloud} are highly statistically significant with
586 small errors in all cases (p-values <0.001). We have used the regression coefficients to determine the part
587 of the DNA active irradiance trends that are caused by trends in total ozone and cloud cover. We have
588 derived the ozone-related DNA active irradiance trend by multiplying the regression coefficient between
589 DNA active irradiance and ozone (β_{O_3}) with the trend in ozone for the period 2050–2099. Accordingly, we
590 derived the respective cloud-related DNA active irradiance trend by multiplying the regression coefficient
591 β_{cloud} with the cloud trend.

592 For the northern high latitude stations (>55º N), we estimate an ozone-related DNA active irradiance trend
593 of about −0.72% per decade, indicating that ~39% of the DNA active irradiance trend (−1.86% per decade)
594 is caused by the trends in ozone. The respective cloud-related DNA active irradiance trend is smaller
595 (−0.21% per decade), which means that the cloud trend explains ~11% of the DNA active irradiance trend.
596 Both parameters account for ~50% of the predicted DNA active irradiance trend. The remaining part of the
597 DNA active irradiance trend is related to changes in other parameters, as for instance in surface albedo, as
598 is discussed later in Section 3.4.

599 Similar results regarding the contribution of ozone and cloud trends to the predicted DNA active irradiance
600 trend are also found for the southern high latitude stations (>55º S), but not for the stations averaged
601 between 50º N and 50º S. The results are summarized in Table 6b. For the southern high latitude stations
602 (>55º S), the ozone-related DNA active irradiance trend is −0.57% per decade and the cloud-related DNA
603 active irradiance trend is +0.07% per decade. As such, ~59% of the DNA active irradiance trend (−0.96%
604 per decade) is explained by ozone, and ~7% is explained by clouds.

605 For stations averaged between 50º N–50º S, we estimate that the ozone-related DNA active irradiance trend
606 is +0.27% per decade, and the cloud-related DNA active irradiance trend is +0.33% per decade. The
607 contribution of changes in cloudiness is larger than the contribution of changes in ozone (~41% compared
608 to ~33%, respectively), and therefore, our findings support the previous results by Eleftheratos et al. (2020),
609 who analyzed a smaller number of GB stations between 50º N–50º S than those used here.

3.4 Changes in surface albedo and relation to DNA active irradiance

In the previous section we showed that DNA active irradiance will continue to decrease after the year 2050 at high latitudes as a result of ozone change rather than cloud cover change. Another parameter affecting the solar UV variability at high latitudes is surface albedo (Weihs et al., 1999; Nichol et al., 2003; Weatherhead et al., 2005; Gröbner, 2012; Bais et al., 2019). In this respect, changes in surface albedo are expected to affect the long-term variability of surface UV-B irradiance. Figure 6 shows the changes in surface albedo simulated with the EMAC CCM at the two stations, Barrow in Alaska and Palmer in Antarctica. More specifically the figure shows the differences between the two model simulations, the one with increasing GHGs (REF) and the one with fixed GHGs (FIX), in order to account also for the effect of increasing GHGs on surface albedo changes according to the methodology applied in Section 3.2. The results refer to the summer seasons of the two hemispheres, where there is sufficient sunlight in the Arctic and the Antarctic. Table 7 summarizes the trends in the differences between the two model simulations, REF and FIX, for the DNA active irradiance, total ozone, cloud cover and surface albedo at Barrow (Alaska) and Palmer (Antarctica) for the periods 1960–1999, 2000–2049 and 2050–2099. While variations in surface albedo are certainly of primary importance for high-latitude sites, they can play a non-negligible role even at mid-latitudes. However, they were not analyzed here.

From Figure 7 it is clear that surface albedo decreases significantly by the end of the 21st century in view of the increasing GHG emissions. The decreases in surface albedo (Table 7) are larger in Barrow (Alaska) than Palmer (Antarctica). The trend for Barrow is qualitatively consistent with the conclusion by Bernhard (2011), showing that the ground at Barrow is covered by snow later and later at the start of winter. We also note that both, Barrow and Palmer, are coastal sites and are heavily affected by local conditions (e.g., how far sea ice gets to the station), which may not be simulated correctly. Therefore, we point out that the evolution of albedo at the two stations shown in Figure 7 is representative for regional changes but may not accurately reflect changes at the exact location of these stations.

To assess the impact of the albedo changes on UV variability, we used surface albedo as additional explanatory variable in the MLR model of Eq. (7). We determined an additional regression coefficient, namely β_{albedo}, which explains the effect of albedo change on DNA active irradiance change at the two stations under study, Barrow and Palmer. We estimated an albedo-related DNA active irradiance trend, in the same way as described above, by multiplying the coefficient β_{albedo} with the trend in albedo differences between the two model simulations.

For Barrow, we estimate an ozone-related DNA active irradiance trend of about −0.87% per decade for the period 2050–2099, indicating that ~41% of the DNA active irradiance trend (−2.14% per decade) is caused by trends in ozone. The respective cloud-related DNA active irradiance trend is about −0.49% per decade, which means that the cloud trend explains ~23% of the DNA active irradiance trend. The surface albedo-related DNA radiation trend is about −0.45% per decade, explaining ~21% of the DNA active irradiance trend in the period 2050-2099. The model suggests that all parameters together explain ~85% of the DNA

646 active irradiance trend, which however may not be such an unbiased result. This is because the effects of
647 clouds and albedo are not independent, as assumed in the regression equation. For 100% albedo and non-
648 absorbing clouds, clouds would barely attenuate UV radiation. For actual albedo and cloud conditions,
649 clouds do attenuate, but the effect is greatly reduced by surface albedo because of multiple reflections
650 between surface and cloud (Nichol et al., 2003).

651 At Palmer, the trends are smaller. The ozone-related DNA active irradiance trend is −0.46% per decade, the
652 cloud-related DNA active irradiance trend is 0.43% per decade, and the albedo-related DNA active
653 irradiance trend is −0.31% per decade. These trends together determine the small negative trend, which is
654 predicted for the DNA active UV irradiance in the period 2050–2099 of about −0.33% per decade.

655 The above calculations indicate that the impact of albedo trends on DNA active irradiance trends due to the
656 continuous increase of GHGs until the end of the 21st century is important and should not be ignored when
657 studying the long-term changes of DNA active radiation reaching the ground. The model simulations at
658 Barrow and Palmer suggest that the surface albedo changes might be larger at Barrow than Palmer
659 according to Table 7. The model simulations also suggest that the northern high latitudes might experience
660 larger changes in surface albedo than the southern high latitudes in the period 2050–2100 (Appendix C,
661 Figures C1 and C2).

662 In order to better represent the northern and southern high latitudes, we also applied the MLR model to the
663 large-scale zonal means of 55º – 75º N and 55º – 75º S. For the northern high latitude zone, the findings are
664 in the same direction as those found for Barrow. We estimate that ~31% of the DNA active irradiance trend
665 is attributable to the trend in total ozone, and that ~14% and ~32% of the DNA active irradiance trend are
666 explained by trends in clouds and surface albedo, respectively. For the southern high latitude zone, we
667 estimate that the largest part of the DNA active irradiance trend is explained by the trend in total ozone, and
668 that the contributions of cloud and albedo trends are small.

669 **4 Summary and Conclusions**

670 We have studied changes in ozone, DNA active irradiance and cloud cover due to the evolution of
671 greenhouse gas concentrations in the near global mean (50° N–50° S) and in the northern and southern high
672 latitudes, using the EMAC CCM simulations from 1960 to 2100.

673 The model simulations have been evaluated against ground-based UV irradiance measurements, satellite
674 ozone observations from SBUV (v8.7) and satellite cloud fraction data from MODIS/Terra for the period
675 2000–2018. The evaluation results can be summarized as follows:

676 • Simulations of total ozone with specified dynamics (RC1SD-base-10 and HIS-SD) reproduce
677 extremely well the variability of total ozone in the northern and southern high latitudes for the
678 periods 1979–2013 and 2000–2018, respectively. The correlation analysis results between EMAC
679 HIS-SD simulation and SBUV (v8.7) satellite ozone de-seasonalized data are: Northern high

680   latitudes (3 station mean), R = +0.899, p-value <0.0001; Southern high latitudes (4 station mean),

681   R = +0.892, p-value <0.0001; 50º N–50º S (13 station mean), R = +0.894, p-value <0.0001.

682 - The respective simulations of DNA active irradiance correlate quite well with ground-based UV

683   measurements, as follows: Northern high latitudes (3 station mean), R = +0.504, p-value <0.0001;

684   Southern high latitudes (4 station mean), R = +0.746, p-value <0.0001; 50º N–50º S (13 station

685   mean, R = +0.499, p-value <0.0001).

686 - Evaluation of cloud cover simulations against MODIS/Terra cloud fraction data gave good

687   correlations as follows: Northern high latitudes (3 stations mean), R = +0.453, p-value <0.0001;

688   Southern high latitudes (4 station mean), R = +0.485, p-value <0.0001; 50º N–50º S, R = +0.703,

689   p-value <0.0001.

690 Between 50º N–50º S, the DNA-damaging UV radiation is expected to decrease until 2050 and to increase

691 thereafter. This increase is associated with expected decreases in cloud cover and insignificant trends in

692 total ozone, as it was shown previously by Eleftheratos et al. (2020). Our study however expands the

693 previous work by adding more stations in low and mid-latitudes and by including estimates from high

694 latitude stations with long-term measurements of UV irradiance.

695 In contrast to the predictions for 50º N–50º S, we estimate that DNA active irradiance will continue to

696 decrease after the year 2050 in the northern and southern high latitudes (>55º) due to increasing ozone.

697 More specifically, for the northern high latitude stations we estimate that total ozone will increase by $1.8 \pm$

698 0.8% from 2050 to 2100, DNA active irradiance will decrease by $8.2 \pm 3.8\%$ and that cloud cover will

699 increase insignificantly by $1.4 \pm 1.3\%$. Similarly, in the southern high latitude stations, total ozone is

700 estimated to increase by $4.2 \pm 2.1\%$ from 2050 to 2100, DNA active irradiance is estimated to decrease by

701 $4.8 \pm 2.9\%$ and cloud cover will decrease insignificantly by $1.1 \pm 1.7\%$.

702 The statistical results have been confirmed by statistical tests. Statistical comparisons of the regression

703 slopes before and after 2050 in the northern and southern high latitude stations under study showed that

704 there are no statistically significant different trends in DNA active irradiance before and after that year. On

705 the other hand, between 50º N–50º S the trends before and after 2050 were found to be statistically

706 significantly different at the 0.05 significance level. The test confirmed the statistical result that DNA

707 active irradiance will reverse sign and become positive after 2050 at stations between 50º N–50º S mainly

708 due to cloud cover and total ozone changes associated with climate change, something that is likely not to

709 happen at high latitudes, where the DNA-damaging UV-B radiation is projected to continue its downward

710 trend after 2050 mainly due to the continued increase of ozone from the reduction of ODSs. In addition, it

711 should be mentioned, that the enhanced GHG concentrations will cool the stratosphere and therefore the

712 stratospheric ozone content (especially in the middle and upper stratosphere) is expected to increase

713 because the ozone depleting reactions (homogeneous gas phase reactions) will be getting slower. From

714 Dhomse et al. (2018) we know that the (future) Arctic and the Antarctic stratosphere are developing

715 differently in spring. In particular, the Arctic region is indicating a stronger reaction on enhanced GHG

716 concentrations (most likely due to the dynamic feedbacks in the northern hemisphere, i.e., related to the
717 planetary wave activity).

718 We clarify here that our findings for the high latitudes refer to the summer periods and not to the seasons
719 when ozone depletion occurs, for which it has been shown that climate change will favor large spring loss
720 of Arctic column ozone in connection with extraordinary (persistent) cold stratospheric winters (with low
721 planetary wave activity) in the future (von der Gathen et al., 2021). The best agreement between the REF
722 simulation results and satellite measurements during the period of ozone depletion was found for the
723 southern high latitudes. The REF simulation (full chemistry and increasing GHGs according to RCP-6.0)
724 seems to underestimate the observed ozone depletion of the 1980s and 1990s for the near global mean (50°
725 N–50° S) and at high latitudes of the Northern Hemisphere. This might at least partly be caused by not
726 considering all ODSs, but only a subset (only CFC-11 and CFC-12 were considered). Despite this feature,
727 the simulated ozone declines during 1979–1999 and the minimum ozone values calculated by the model in
728 the 1990s for the northern mid- and high latitudes, are qualitatively in line with the satellite ozone
729 observations.

730 Also, our analysis suggests that clouds might stay constant over the Arctic, while other models predict that
731 cloud cover in the Arctic will increase during the next decades due to enhanced evaporation of water vapor
732 by the sea-ice decrease. Our estimates, however, refer to two sites in the Arctic and not to the entire Arctic
733 Ocean. As such, our results should be considered representative of the land sites under study and not of the
734 entire Arctic or Antarctic regions. In addition, we cannot reliably evaluate the projection of cloud cover
735 over time, using MODIS observations for a relatively short period. So, in the end we must trust that the
736 physics coded in the model is correct. Hence, verification of our results using independent CCMs would be
737 highly desired. We conducted a separate analysis on total cloud cover variability and trends through the 21st
738 century, using the available simulations from the CCMI-1 REF-C2 set, which showed that the EMAC CCM
739 results fall well within the range of uncertainty (i.e., $\pm 2\sigma$), close to the ensemble average ($\pm 1\sigma$).

740 Moreover, we applied a multiple linear regression model to examine the contribution of ozone and cloud
741 trends to the estimated DNA active irradiance trends after the year 2050. The model was applied to the
742 differences between the two model simulations, REF and FIX. It was found that ozone is the primary
743 contributor accounting for about ~50% of the predicted trends in DNA active irradiance after 2050 both in
744 the northern and in the southern high latitude stations.

745 The impact of surface albedo on DNA active irradiance trends due to the evolution of GHGs (RCP-6.0) has
746 been examined at two stations, Barrow in the Arctic, and Palmer in the Antarctic. The model simulations
747 suggest that declining trends in surface albedo are larger at Barrow than Palmer. The driving force for the
748 decrease in Arctic surface albedo is by 70% the decrease in snow cover fraction over the Arctic land and
749 sea-ice due to the increase in surface air temperature and decrease in snowfall (Zhang et al., 2019).

750 Unlike the Arctic sea-ice, which has consistently declined over the past four decades, the Antarctic sea-ice
751 has shown little change (increase) from 1979 to 2015 but large regional and temporal variability (Maksym,

2019). A rapid decline in 2015–2018, far exceeding the decreasing rates seen in the Arctic (Parkinson, 2019), may have foreboded future changes in Antarctic sea-ice (Eayrs et al., 2021). The observed decline lowered the region's surface albedo, highlighting the importance of Antarctic sea-ice loss to the global snow and ice albedo feedback (Riihelä et al., 2021). This sea-ice reduction probably resulted from the interaction of a decades-long ocean warming trend and an early spring southward advection of atmospheric heat, with an exceptional weakening of the Southern Hemisphere mid-latitude westerlies in late spring (Eayrs et al., 2021). Obviously, such abrupt declines cannot be predicted by the present-day model simulations. This is because the mechanisms for the Antarctic sea-ice variations are not yet well understood and future predictions are highly uncertain.

IPCC (2021) concluded that there has been no significant trend in Antarctic sea-ice area from 1979 to 2020, due to regionally opposing trends and large internal variability. In the Bellingshausen and Amundsen Seas, however, the observed sea-ice has shown decreasing trends (Maksym, 2019; Parkinson, 2019; Eayrs et al., 2021). Our estimates for Palmer, which is located at the coast of the Bellingshausen Sea, shows a negative trend in surface albedo from 1979 to 2020, which is in line with the negative trends in sea-ice observed in Bellingshausen and Amundsen Seas. The REF simulation shows that the surface albedo at Palmer will continue to decrease until 2100. This result should be considered representative of the Palmer station and its surroundings, and not of the entire Antarctic region.

The key findings presented in this study are that model and measurements agree fairly well, giving support to the simulations of the future scenarios. Cloud cover is generally decreasing, leading to increased solar radiation, apart from the high latitudes, where no significant changes are observed. Total ozone shows an increasing trend due to the reduction of ODSs, while a decrease is observed after 2050 on a near-global scale due to the increasing GHGs. UV trends are a combination of changes in ozone and cloud cover, while at high latitudes, the decreasing surface albedo in the second half of the 21st century has a significant influence on the surface UV radiation.

The above findings were based on the analysis of model simulations from 3 stations in the northern high latitudes, 4 stations in the southern high latitudes, and 13 stations in the near-global mean with contributions mainly from the mid-latitudes. A separate analysis using zonal means showed that the results from the analysis of the model data averaged over geographical zones are qualitatively in the same direction with those of the station averages. All simulations were based on a single CCM, and therefore, verification of the results from simulations of other models would be quite useful.

Appendix A Qualitative evaluation of free running CCM simulations against simulations with specified dynamics

In this appendix, we compare the free running ozone simulation REF, with the SD simulation RC1SD-base-10 and SBUV satellite ozone data (v8.7). The simulation with specific dynamics RC1SD-base-10 covers the period January 1979 – December 2013. The simulation has been used in recent assessments reports for

787 stratospheric ozone studies (e.g., LOTUS, 2019). In addition to the nudging towards ECMWF ERA-Interim
788 (Dee at al., 2011) reanalysis data (for details about the nudging setup see Jöckel et al., 2016) the simulation
789 uses also sea surface temperatures and sea-ice concentrations from the ERA Interim reanalysis data. Here,
790 we use the SD simulation (RC1SD-base-10) to show that the free running simulation (REF) is capable to
791 qualitatively reflect the negative ozone trends of the 1980s and 1990s. The reason for quoting the RC1SD-
792 base-10 simulation is because the HIS-SD simulation that is used in section 3.1 does not go back in time
793 before 2000, and therefore we cannot qualitatively evaluate our free running simulation before 2000. We
794 also appose here the SD simulation (HIS-SD), which covers the period January 2000 – July 2018. This is
795 useful and helpful to classify the results of the free running model system concerning the quality with
796 respect to the SD simulation and the observations of the stations, and it serves as a "bridge" from the
797 observations via the SD simulation results, to the results of the (longer-term) free-running model
798 simulation.

799 Figure A1 shows the comparison between the simulations and SBUV data. Obviously, the RC1SD-base-10
800 simulation (period 1979–2013) compares much better with the SBUV data than the REF simulation. The
801 same also holds for the HIS-SD simulation (period 2000–2018). This is expected since the SD simulation
802 uses reanalyzed meteorology, whereas the free running simulation has its own meteorological/synoptical
803 sequence. For comparison with the fixed GHG simulation, we need to switch to the pair of free running
804 simulations. And the question is, if the evaluation (comparison with observations) also hold for the REF
805 simulation, which is the basis for the comparison with the fixed GHG simulation (FIX). In the case of free
806 running simulations, the evaluation is only possible for the trends and for the amplitude of the year-to-year
807 variability, but not for the sign of the anomaly in a given nominal year and/or month. Figure A1 shows that
808 the free running simulation (REF) reflects correctly the negative ozone trends of the past, seen in the
809 observations and in the SD simulation, and is therefore suitable for comparison with the fixed GHG
810 simulation.

811
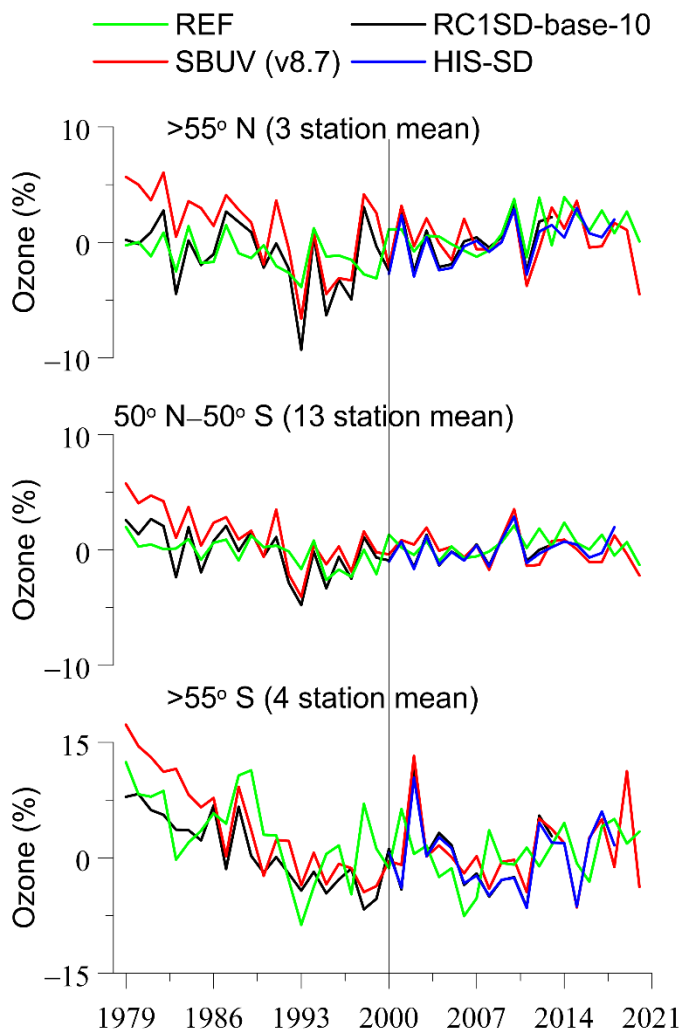
Figure A1. Comparison of REF (free running simulation; green line) with RC1SD-base-10 (SD simulation for 1979–2013; black line), HIS-SD (SD simulation for 2000–2018; blue line) and SBUV (v8.7) satellite measurements (red line) for 3 stations higher than 55º N (upper plot), 13 stations between 50º N–50º S (middle plot) and 4 stations higher than 55º S (lower plot). The vertical line has been put in the year 2000. The y-axis shows yearly averaged total ozone data (in %) calculated from de-seasonalized monthly data. The monthly data were de-seasonalized relative to the long-term monthly mean (2000–2018) and were expressed in %. For the northern high latitude stations, the annual average refers to the average of monthly anomalies from March to September, and for the southern high latitude stations, it refers to the average of monthly anomalies from September to March. For the stations between 50º N–50º S we used all months to calculate the annual average.

824 **Appendix B Model simulations of zonally averaged cloud cover between 50º and 80º N**

825 Figure B1 shows the changes of the zonally averaged cloud cover based on REF (RCP-6.0) and FIX

826 simulations, and their differences (REF minus FIX), per 10-degree latitude zones from 50º to 80º N. For the

827 period 1960 to 2100, the changes in cloud cover due to the evolution of GHGs (RCP-6.0) are presented in

828 Table B1. The same picture with increasing trends as we move northward of 50º N is also found for the

829 period 2050 to 2100.

830

831 **Table B1.** Changes in zonal mean cloud cover between 50º and 80º N due to the evolution of GHGs (RCP-

832 6.0), for the periods 1960–2100 and 2050–2100.

	1960–2100			2050–2100		
	% Change	p-value	N	% Change	p-value	N
50º–60º N	0.9	< 0.0001	140	0.3	0.56064	50
60º–70º N	2.7	< 0.0001	140	0.7	0.27113	50
70º–80º N	4.3	< 0.0001	140	1.9	0.00012	50

833

(a)   (b)
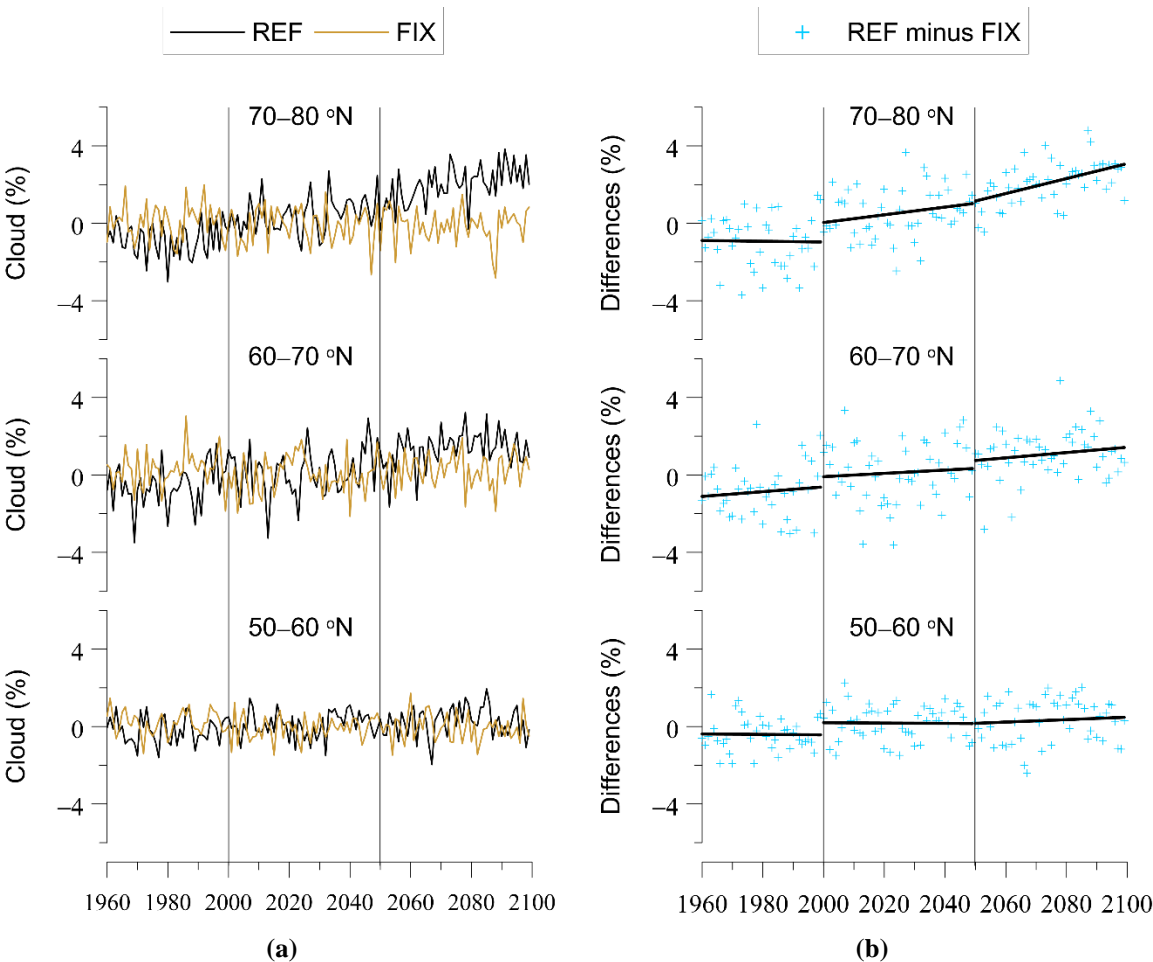
834 **Figure B1.** EMAC CCM projections of zonal mean cloud cover for 10-degree latitude zones (50º–60º N,

835 60º–70º N, 70º–80º N), based on simulations with increasing and fixed GHGs mixing ratios. **(a)** REF is the

836 simulation with increasing GHGs according to RCP-6.0. FIX is the simulation with fixed GHGs emissions

837 at 1960 levels. **(b)** Difference between the two model simulations, as an indicator of the impact of

838 increasing GHGs. The y-axis in the left figure (a) shows yearly averaged cloud cover data (in %) calculated

839 from de-seasonalized monthly data. The monthly data were de-seasonalized relative to the long-term

840 monthly mean (1990–2019) and were expressed in %. For the northern high latitudes, the annual average

841 refers to the average of monthly anomalies from March to September.

842

843 **Appendix C Model simulations of zonally averaged surface albedo between 50º and 80º N, and 50º**
844 **and 80º S**

845 Figure C1 shows the changes in zonally averaged surface albedo based on REF (RCP-6.0) and FIX

846 simulations, and their differences (REF minus FIX), per 10-degree latitude zones between 50º N and 80º N.

847 Figure C2 shows the respective changes between 50º S and 80º S. The changes in surface albedo due to the

848 evolution of GHGs (RCP-6.0) between 50º and 80º N, and 50º and 80º S, are summarized in Table C1.

849

850 **Table C1.** Changes in zonal mean surface albedo due to the evolution of GHGs (RCP-6.0) between 50º and

851 80º N, and 50º and 80º S, for the periods 1960–2100 and 2050–2100.

North	1960–2100			2050–2100		
	% Change	p-value	N	% Change	p-value	N
50º–60º N	−21.0	< 0.0001	140	−8.9	< 0.0001	50
60º–70º N	−18.3	< 0.0001	140	−9.2	< 0.0001	50
70º–80º N	−41.3	< 0.0001	140	−15.1	< 0.0001	50

852

South	1960–2100			2050–2100		
	% Change	p-value	N	% Change	p-value	N
50º–60º S	−12.5	< 0.0001	140	−3.7	0.00299	50
60º–70º S	−22.5	< 0.0001	140	−3.8	0.00298	50
70º–80º S	−6.1	< 0.0001	140	−1.3	0.00132	50

853

854
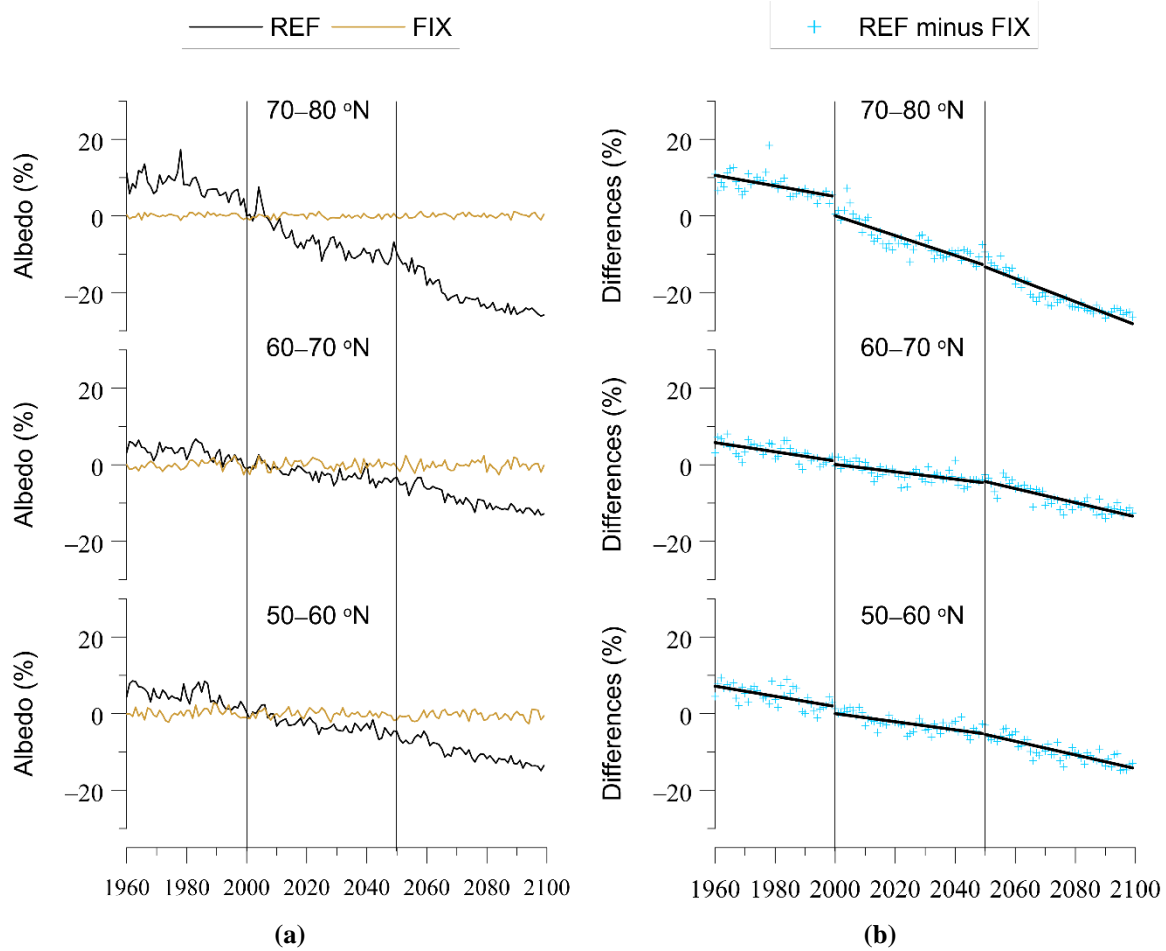
Figure C1. EMAC CCM projections of zonal mean surface albedo for 10-degree latitude zones (50-60º N, 60-70º N, 70-80º N), based on simulations with increasing and fixed GHGs mixing ratios. **(a)** REF is the simulation with increasing GHGs according to RCP-6.0. FIX is the simulation with fixed GHGs emissions at 1960 levels. **(b)** Difference between the two model simulations, as an indicator of the impact of increasing GHGs. The y-axis in the left figure (a) shows yearly averaged surface albedo data (in %) calculated from de-seasonalized monthly data. The monthly data were de-seasonalized relative to the long-term monthly mean (1990–2019) and were expressed in %. For the northern high latitudes, the annual average refers to the average of monthly anomalies from March to September.
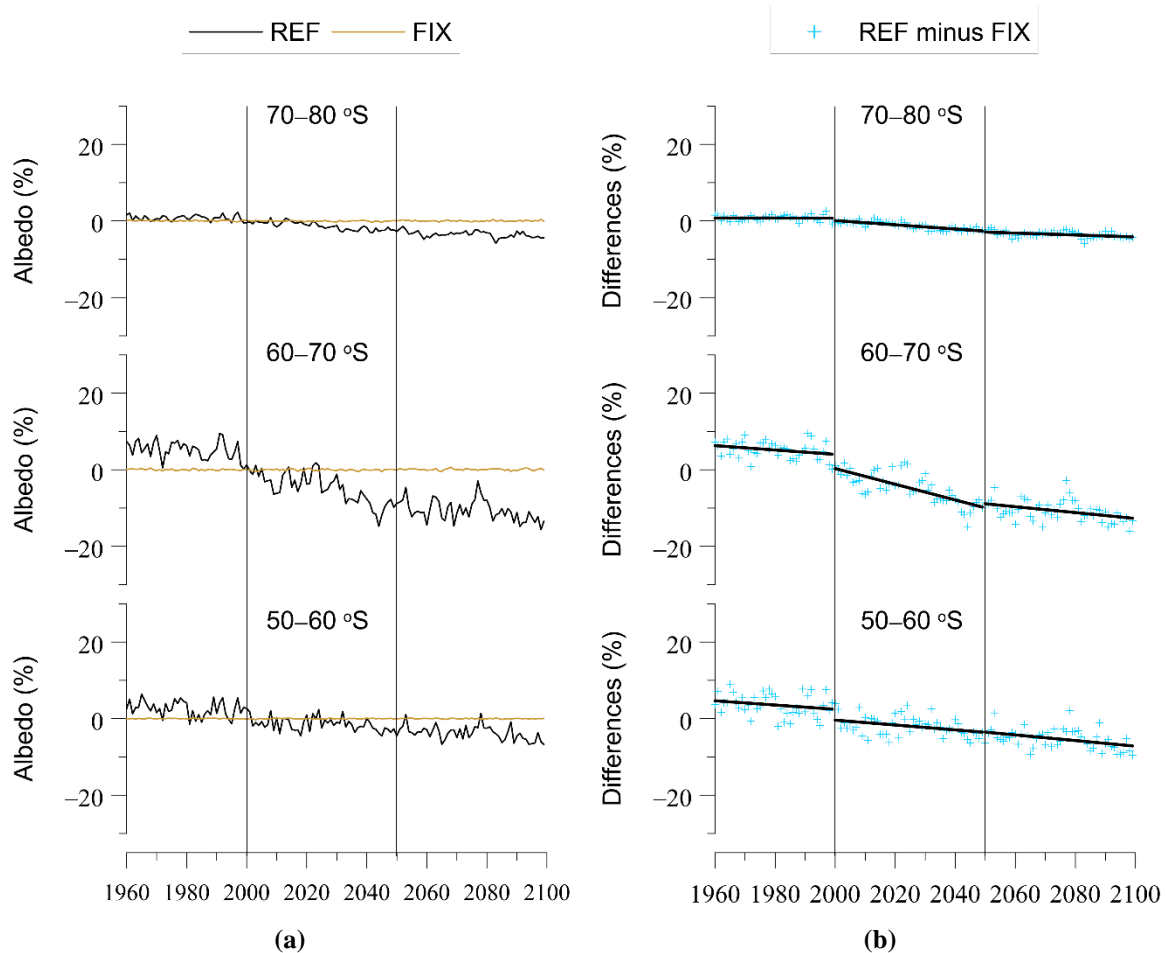
Figure C2. Same as Figure C1 but for 50-60º S, 60-70º S, and 70-80º S. The y-axis in the left figure (a) shows yearly averaged surface albedo data (in %) calculated from de-seasonalized monthly data. The monthly data were de-seasonalized relative to the long-term monthly mean (1990–2019) and were expressed in %. For the southern high latitudes, the annual average refers to the average of monthly anomalies from September to March.

Data Availability: The UV irradiance data are archived at the NDACC data repository, https://www-air.larc.nasa.gov/pub/NDACC/PUBLIC/stations/ (last access 4 September 2022). The SBUV (v8.7) satellite ozone data are available at https://acd-ext.gsfc.nasa.gov/Data_services/merged/previous_mods.html (last access 4 September 2022). The MODIS/Terra v6.1 satellite cloud fraction monthly mean data (MOD08_M3 v6.1) are available at https://giovanni.gsfc.nasa.gov/giovanni/#service=TmAvMp&starttime=&endtime=&data=MOD08_M3_6_1_Cloud_Fraction_Mean_Mean (last access 4 September 2022).

879 **Author Contribution:** K.E. and C.Z. conceptualized the study. A.B., G.B., D.K., S.S., B.L., C.B., F.A.,
880 S.S., H.D., and K.L. provided ground-based UV irradiance data. K.E., D.K., I.F. and K.T. analysed data.
881 M.D. and P.J. provided the EMAC model simulations. J.K. and K.D. processed the model simulations. The
882 manuscript was originally prepared by K.E. and was reviewed with comments and corrections from all co-
883 authors.

884 **Competing interests:** One co-author (MD) is coordinator, and one co-author (IP) is co-organizer of the
885 special issue "Atmospheric ozone and related species in the early 2020s: latest results and trends
886 (ACP/AMT inter-journal SI), 2021".

887

888 **Acknowledgments:** The research work was partially funded by the Hellenic Foundation for Research and
889 Innovation (H.F.R.I.) under the "First Call for H.F.R.I. Research Projects to support Faculty members and
890 Researchers and the procurement of high-cost research equipment grant" (Atmospheric parameters
891 affecting SPectral solar IRradiance and solar Energy (ASPIRE), Project Number: 300). We acknowledge
892 support by the project "PANhellenic infrastructure for Atmospheric Composition and climatE change"
893 (MIS 5021516) which is implemented under the Action "Reinforcement of the Research and Innovation
894 Infrastructure", funded by the Operational Programme "Competitiveness, Entrepreneurship and Innovation"
895 (NSRF 2014-2020), and co-financed by Greece and the European Union (European Regional Development
896 Fund). The research contributes to the National Network for Climate Change and its Impact – CLIMPACT.
897 We acknowledge the project Long-term Ozone Trends and Uncertainties in the Stratosphere (LOTUS) and
898 the Mariolopoulos-Kanaginis Foundation for the Environmental Sciences. The EMAC simulations have
899 been performed at the German Climate Computing Centre (DKRZ) through support from the
900 Bundesministerium für Bildung und Forschung (BMBF). DKRZ and its scientific steering committee are
901 gratefully acknowledged for providing the HPC and data archiving resources for this consortial project
902 ESCiMo (Earth System Chemistry integrated Modelling). Measurements of French spectroradiometers are
903 supported by CNES (French programme TOSCA); the Université de La Réunion and CNRS; the Région
904 Hauts-de-France and the Ministère de l'Enseignement Supérieur et de la Recherche (CPER Climibio); and
905 the European Fund for Regional Economic Development. Technicians at the three French and at the
906 Finnish (Sodankylä) sites are acknowledged for the maintenance and calibration of the instruments. Kaisa
907 Lakkala is supported by the CHAMPS project (grant no. 329225) of the Academy of Finland under the
908 CLIHE programme. We acknowledge the SBUV science team for providing the satellite ozone profiles.
909 NIWA UV spectrometer systems, serial numbers UV3 (Mauna Loa, HI) and UV5 (Boulder, CO) in the
910 USA are owned and operated by NOAA/ESRL/Global Monitoring Division, Boulder CO. They are
911 maintained, calibrated, and operated by NOAA. The final data from both of these instruments are quality
912 controlled and produced by NIWA-Lauder, New Zealand. We thank NIWA and NOAA for the use of their
913 data in this publication. Analyses and visualizations used in this study were produced with the Giovanni
914 online data system, developed and maintained by the NASA GES DISC. We also acknowledge the MODIS
915 mission scientists and associated NASA personnel for the production of the data used in this research

916 effort. We would like to thank the anonymous reviewer for summarizing the key findings which we
917 incorporated at the end of the conclusions.

918 **References**

919 Armitage, P., Berry, G., and Matthews, J. N. S.: Statistical methods in medical research, 4th edition,
920 Blackwell Publishing, ISBN 0-632-05257-0, pp.865, 2002.

921 Bais, A. F., Bernhard, G., McKenzie, R. L., Aucamp, P. J., Young, P. J., Ilyas, M., Jöckel, P., and Deushi,
922 M.: Ozone-climate interactions and effects on solar ultraviolet radiation, Photochem. Photobiol. Sci., 18,
923 602-640, https://doi.org/10.1039/C8PP90059K, 2019.

924 Bais, A. F., McKenzie, R. L., Bernhard, G., Aucamp, P. J., Ilyas, M., Madronich, S., and Tourpali, K.:
925 Ozone depletion and climate change: impacts on UV radiation, Photochem. Photobiol. Sci., 14(1), 19–52,
926 doi:10.1039/c4pp90032d, 2015.

927 Bais, A. F., Tourpali, K., Kazantzidis, A., Akiyoshi, H., Bekki, S., Braesicke, P., Chipperfield, M. P.,
928 Dameris, M., Eyring, V., Garny, H., Iachetti, D., Jöckel, P., Kubin, A., Langematz, U., Mancini, E.,
929 Michou, M., Morgenstern, O., Nakamura, T., Newman, P. A., Pitari, G., Plummer, D. A., Rozanov, E.,
930 Shepherd, T. G., Shibata, K., Tian, W., and Yamashita, Y.: Projections of UV radiation changes in the 21st
931 century: impact of ozone recovery and cloud effects, Atmos. Chem. Phys., 11, 7533–7545,
932 https://doi.org/10.5194/acp-11-7533-2011, 2011.

933 Bais, A. F., and Zerefos C. S.: The effect of changes in ozone on solar UV-B radiation at Reykjavik, SPIE
934 Vol. 2049 Atmospheric Radiation, 263–267, 1993.

935 Bais, A. F., Zerefos, C. S., Meleti, C., Ziomas I. C., and Tourpali, K.: Spectral measurements of solar UVb
936 radiation and its relations to total ozone, SO_2, and clouds, J. Geophys. Res., 98(D3), 5199–5204, 1993.

937 Bernhard, G.: Trends of solar ultraviolet irradiance at Barrow, Alaska, and the effect of measurement
938 uncertainties on trend detection, Atmos. Chem. Phys., 11, 13029–13045, https://doi.org/10.5194/acp-11-
939 13029-2011, 2011.

940 Bernhard, G., Booth, C. R., Ehramjian, J. C., Stone, R., and Dutton, E. G.: Ultraviolet and visible radiation
941 at Barrow, Alaska: Climatology and influencing factors on the basis of version 2 National Science
942 Foundation network data, J. Geophys. Res., 112, D09101, doi:10.1029/2006JD007865, 2007.

943 Bernhard, G., Mayer, B., Seckmeyer, G., and Moise, A.: Measurements of spectral solar UV irradiance in
944 tropical-Australia, J. Geophys. Res. Atmospheres, 102(D7), 8719 – 8730,
945 https://doi.org/10.1029/97JD00072, 1997.

946 Bernhard, G., Neale, R. E., Barnes, P. W., Neale, P. J., Zepp, R. G., Wilson, S. R., Andrady, A. L., Bais, A.
947 F., McKenzie, R. L., Aucamp, P. J., Young, P. J., Liley, J. B., Lucas, R. M., Yazar, S., Rhodes, L. E.,
948 Byrne, S. N., Hollestein, L. M., Olsen, C. M., Young, A. R., Robson, T. M., Bornman, J. F., Jansen, M. A.

949 K., Robinson, S. A., Ballaré, C. L., Williamson, C. E., Rose, K. C., Banaszak, A. T., Häder, D.-P.,
950 Hylander, S., Wängberg, S.-Å., Austin, A. T., Hou, W.-C., Paul, N. D., Madronich, S., Sulzberger, B.,
951 Solomon, K. R., Li, H., Schkowski, T., Longstreth, J., Pandey, K. K., Heikkilä, A. M., and White, C. C.:
952 Environmental effects of stratospheric ozone depletion, UV radiation and interactions with climate change:
953 UNEP Environmental Effects Assessment Panel, update 2019, Photochem. Photobiol. Sci., 19, 542–584,
954 doi:10.1039/d0pp90011g, 2020.

955 Bernhard, G., and Stierle, S.: Trends of UV Radiation in Antarctica, Atmosphere, 11(8), 795,
956 https://doi.org/10.3390/atmos11080795, 2020.

957 Bhartia, P. K., McPeters, R. D., Flynn, L. E., Taylor, S., Kramarova, N. A., Frith, S., Fisher, B., and
958 DeLand, M.: Solar Backscatter UV (SBUV) total ozone and profile algorithm, Atmos. Meas. Tech., 6,
959 2533–2548, https://doi.org/10.5194/amt-6-2533-2013, 2013.

960 Blumthaler M., and Ambach, W.: Indication of increasing solar ultraviolet-B radiation flux in alpine
961 regions, Science, 248(4952), 206-208, doi: 10.1126/science.2326634, 1990.

962 Brühl, C., and Crutzen, P. J.: On the disproportionate role of tropospheric ozone as a filter against solar
963 UV-B radiation, Geophys. Res. Lett., 16, 703–706, 1989.

964 Butchart, N.: The Brewer-Dobson circulation, Rev. Geophys., 52, doi:10.1002/2013RG000448, 2014.

965 Collins, W. J., Bellouin, N., Doutriaux-Boucher, M., Gedney, N., Halloran, P., Hinton, T., Hughes, J.,
966 Jones, C. D., Joshi, M., Liddicoat, S., Martin, G., O'Connor, F., Rae, J., Senior, C., Sitch, S., Totterdell, I.,
967 Wiltshire, A., and Woodward, S.: Development and evaluation of an Earth-System model – HadGEM2,
968 Geosci. Model Dev., 4, 1051–1075, doi:10.5194/gmd-4-1051-2011, 2011.

969 Dee, D. P., Uppala, S. M., Simmons, A. J., Berrisford, P., Poli, P., Kobayashi, S., Andrae, U., Balmaseda,
970 M. A., Balsamo, G., Bauer, P., Bechtold, P., Beljaars, A. C. M., van de Berg, L., Bidlot, J., Bormann, N.,
971 Delsol, C., Dragani, R., Fuentes, M., Geer, A. J., Haimberger, L., Healy, S. B., Hersbach, H., Hólm, E. V.,
972 Isaksen, L., Kållberg, P., Köhler, M., Matricardi, M., McNally, A. P., Monge-Sanz, B. M., Morcrette, J.-J.,
973 Park, B.-K., Peubey, C., de Rosnay, P., Tavolato, C., Thépaut, J.-N., and Vitart, F.: The ERA-Interim
974 reanalysis: configuration and performance of the data assimilation system, Q. J. Roy. Meteor. Soc., 137,
975 553–597, doi:10.1002/qj.828, 2011.

976 De Mazière, M., Thompson, A. M., Kurylo, M. J., Wild, J. D., Bernhard, G., Blumenstock, T., Braathen, G.
977 O., Hannigan, J. W., Lambert, J.-C., Leblanc, T., et al. The Network for the Detection of Atmospheric
978 Composition Change (NDACC): History, status and perspectives, Atmos. Chem. Phys., 18, 4935–4964,
979 2018.

980 den Outer, P. N., Slaper, H., Kaurola, J., Lindfors, A., Kazantzidis, A., Bais, A. F., Feister, U., Junk, J.,
981 Janouch, M., and Josefsson, W.: Reconstructing of erythemal ultraviolet radiation levels in Europe for the
982 past 4 decades, J. Geophys. Res., 115, D10102, doi:10.1029/2009JD012827, 2010.

983 Dhomse, S. S., Kinnison, D., Chipperfield, M. P., Salawitch, R. J., Cionni, I., Hegglin, M. I., Abraham, N.
984 L., Akiyoshi, H., Archibald, A. T., Bednarz, E. M., et al.: Estimates of ozone return dates from Chemistry-
985 Climate Model Initiative simulations, Atmos. Chem. Phys., 18, 8409–8438, 2018.

986 Douglass, A., Fioletov, V. (Coordinating Lead Authors), Godin-Beekmann, S., Müller, R., Stolarski, R. S.,
987 Webb, A. (Lead Authors), Arola, A., Burkholder, J. B., Burrows, J. P., Chipperfield, M. P., Cordero, R.,
988 David, C., den Outer, P. N., Diaz, S. B., Flynn, L. E., Hegglin, M., Herman, J. R., Huck, P., Jánosi, I. M.,
989 Krzyscin, J. W., Liu, Y., Logan, J., Matthes, K., McKenzie, R. L., Muthama N. J., Petropavlovskikh, I.,
990 Pitts, M., Ramachandran, S., Rex, M., Salawitch, R. J., Sinnhuber, B.-M., Staehelin, J., Strahan, S.,
991 Tourpali, K., Valverde-Canossa, J., and Vigouroux, C.: Stratospheric ozone and surface ultraviolet
992 radiation. In Scientific assessment of ozone depletion: 2010, Global Ozone Research and Monitoring
993 Project (Report No. 52, Chapter 2). Geneva, Switzerland: World Meteorological Organization, 2011.

994 Eayrs, C., Li, X., Raphael, M. N., and Holland, D. M.: Rapid decline in Antarctic sea ice in recent years
995 hints at future change, Nat. Geosci., 14, 460 – 464, doi:10.1038/s41561-021-00768-3, 2021.

996 Eleftheratos, K., Kazadzis, S., Zerefos, C., Tourpali, K., Meleti, C., Balis, D., Zyrichidou, I., Lakkala, K.,
997 Feister, U., Koskela, T., Heikkilä, A., and Karhu, J. M.: Ozone and spectroradiometric UV changes in the
998 past 20 years over high latitudes, Atmosphere-Ocean, 53, 117-125, doi:10.1080/07055900.2014.919897,
999 2015.

1000 Eleftheratos, K., Kapsomenakis, J., Zerefos, C. S., Bais, A. F., Fountoulakis, I., Dameris, M., Jöckel, P.,
1001 Haslerud, A. S., Godin-Beekmann, S., Steinbrecht, W., Petropavlovskikh, I., Brogniez, C., Leblanc, T.,
1002 Liley, J. B., Querel R., and Swart, D. P. J.: Possible Effects of Greenhouse Gases to Ozone Profiles and
1003 DNA Active UV-B Irradiance at Ground Level, Atmosphere, 11, 228, doi:10.3390/atmos11030228, 2020.

1004 Eyring, V., Lamarque, J.-F., Hess, P., Arfeuille, F., Bowman, K., Chipperfield, M., Duncan, B., Fiore, A.,
1005 Gettelman, A., Giorgetta, M., Granier, C., Hegglin, M., Kinnison, D., Kunze, M., Langematz, U., Luo, B.,
1006 Martin, R., Matthes, K., Newman, P., Peter, T., Robock, A., Ryerson, A., Saiz-Lopez, A., Salawitch, R.,
1007 Schultz, M., Shepherd, T., Shindell, D., Stähelin, J., Tegtmeier, S., Thomason, L., Tilmes, S., Vernier, J.-P.,
1008 Waugh, D., and Young, P.: Overview of IGAC/SPARC Chemistry-Climate Model Initiative (CCMI)
1009 Community Simulations in Support of Upcoming Ozone and Climate Assessments, SPARC Newsletter, 40,
1010 48-46, 2013.

1011 Fountoulakis, I., and Bais, A. F.: Projected changes in erythemal and vitamin D effective irradiance over
1012 northern-hemisphere high latitudes, Photochem. Photobiol. Sci., 14(7), 1251–1264,
1013 doi:10.1039/c5pp00093a, 2015.

1014 Fountoulakis, I., Bais, A. F., Tourpali, K., Fragkos, K. and Misios, S.: Projected changes in solar UV
1015 radiation in the Arctic and sub-Arctic Oceans: Effects from changes in reflectivity, ice transmittance,
1016 clouds, and ozone, J. Geophys. Res. Atmos., 119(13), 8073–8090, doi:10.1002/2014JD021918, 2014.

Fountoulakis, I., Diémoz, H., Siani, A. M., Hülsen, G., and Gröbner, J.: Monitoring of solar spectral ultraviolet irradiance in Aosta, Italy, Earth Syst. Sci. Data, 12, 2787–2810, https://doi.org/10.5194/essd-12-2787-2020, 2020a.

Fountoulakis, I., Diémoz, H., Siani, A.-M., Laschewski, G., Filippa, G., Arola, A., Bais, A. F., De Backer, H., Lakkala, K., Webb, A. R., De Bock, V., Karppinen, T., Garane, K., Kapsomenakis, J., Koukouli, M.-E., and Zerefos, C. S.: Solar UV Irradiance in a Changing Climate: Trends in Europe and the Significance of Spectral Monitoring in Italy, Environments, 7(1), https://doi.org/10.3390/environments7010001, 2020b.

Fountoulakis, I., Zerefos, C. S., Bais, A. F., Kapsomenakis, J., Koukouli, M.-E., Ohkawara, N., Fioletov, V., De Backer, H., Lakkala, K., Karppinen, T., Webb, A. R.: Twenty-five years of spectral UV-B measurements over Canada, Europe and Japan: Trends and effects from changes in ozone, aerosols, clouds, and surface reflectivity, Comptes Rendus Geoscience, 350(7), 393–402, https://doi.org/10.1016/j.crte.2018.07.011, 2018.

Gröbner J.: Ultraviolet Radiation: Distribution and Variability. In: Meyers R.A. (eds) Encyclopedia of Sustainability Science and Technology, Springer, New York, NY, https://doi.org/10.1007/978-1-4419-0851-3_453, 2012.

Jöckel, P., Tost, H., Pozzer, A., Kunze, M., Kirner, O., Brenninkmeijer, C. A. M., Brinkop, S., Cai, D. S., Dyro, C., Eckstein, J., et al.: Earth System Chemistry integrated Modelling (ESCiMo) with the Modular Earth Submodel System (MESSy) version 2.51, Geosci. Model Dev., 9, 1153–1200, 2016.

Jones, C. D., Hughes, J. K., Bellouin, N., Hardiman, S. C., Jones, G. S., Knight, J., Liddicoat, S., O'Connor, F. M., Andres, R. J., Bell, C., Boo, K.-O., Bozzo, A., Butchart, N., Cadule, P., Corbin, K. D., Doutriaux-Boucher, M., Friedlingstein, P., Gornall, J., Gray, L., Halloran, P. R., Hurtt, G., Ingram, W. J., Lamarque, J.-F., Law, R. M., Meinshausen, M., Osprey, S., Palin, E. J., Parsons Chini, L., Raddatz, T., Sanderson, M. G., Sellar, A. A., Schurer, A., Valdes, P., Wood, N., Woodward, S., Yoshioka, M., and Zerroukat, M.: The HadGEM2-ES implementation of CMIP5 centennial simulations, Geosci. Model Dev., 4, 543–570, https://doi.org/10.5194/gmd-4-543-2011, 2011.

IPCC, 2021: Summary for Policymakers. In: Climate Change 2021: The Physical Science Basis. Contribution of Working Group I to the Sixth Assessment Report of the Intergovernmental Panel on Climate Change [Masson Delmotte, V., Zhai, P., Pirani, A., Connors, S. L., Péan, C., Berger, S., Caud, N., Chen, Y., Goldfarb, L., Gomis, M. I., Huang, M., Leitzell, K., Lonnoy, E., Matthews, J. B. R., Maycock, T. K., Waterfield, T., Yelekçi, O., Yu R., and Zhou, B. (eds.)]. Cambridge University Press. In Press.

Kerr, J. B., and McElroy, C. T.: Evidence for large upward trends of ultraviolet-B radiation linked to ozone depletion, Science, 262(5136), 1035–1034, doi:10.1126/science.262.5136.1032, 1993.

Kosmopoulos, P. G., Kazadzis, S., Schmalwieser, A. W., Raptis, P. I., Papachristopoulou, K., Fountoulakis, I., Masoom, A., Bais, A. F., Bilbao, J., Blumthaler, M., Kreuter, A., Siani, A. M., Eleftheratos, K., Topaloglou, C., Gröbner, J., Johnsen, B., Svendby, T. M., Vilaplana, J. M., Doppler, L., Webb, A. R.,

1052 Khazova, M., De Backer, H., Heikkilä, A., Lakkala, K., Jaroslawski, J., Meleti, C., Diémoz, H., Hülsen, G.,
1053 Klotz, B., Rimmer, J., and Kontoes, C.: Real-time UV index retrieval in Europe using Earth observation-
1054 based techniques: system description and quality assessment, Atmos. Meas. Tech., 14, 5657–5699,
1055 https://doi.org/10.5194/amt-14-5657-2021, 2021.

1056 Krzyścin, J. W. and Baranowski, D. B.: Signs of the ozone recovery based on multi sensor reanalysis of
1057 total ozone for the period 1979–2017, Atmospheric Environment, 199, 334–344,
1058 https://doi.org/10.1016/j.atmosenv.2018.11.050, 2019.

1059 Lakkala, K., Arola, A., Heikkilä,A., Kaurola, J., Koskela, T., Kyrö, E., Lindfors, A., Meinander, O.,
1060 Tanskanen, A., Gröbner, J. and Hülsen, G.: Quality assurance of the Brewer spectral UV measurements in
1061 Finland. Atmos. Chem. Phys., 8, 3369-3383, 2008.

1062 Kylling, A., Dahlback, A., and Mayer, B.: The effect of clouds and surface albedo on UV irradiances at a
1063 high latitude site, Geophys. Res. Lett., 27(9), 1411–1414, 2000.

1064 Lamy, K., Portafaix, T., Josse, B., Brogniez, C., Godin-Beekmann, S., Bencherif, H., Revell, L., Akiyoshi,
1065 H., Bekki, S., Hegglin, M. I., Jöckel, P., Kirner, O., Liley, B., Marecal, V., Morgenstern, O., Stenke, A.,
1066 Zeng, G., Abraham, N. L., Archibald, A. T., Butchart, N., Chipperfield, M. P., Di Genova, G., Deushi, M.,
1067 Dhomse, S. S., Hu, R.-M., Kinnison, D., Kotkamp, M., McKenzie, R., Michou, M., O'Connor, F. M.,
1068 Oman, L. D., Pitari, G., Plummer, D. A., Pyle, J. A., Rozanov, E., Saint-Martin, D., Sudo, K., Tanaka, T.
1069 Y., Visioni, D., and Yoshida, K.: Clear-sky ultraviolet radiation modelling using output from the Chemistry
1070 Climate Model Initiative, Atmos. Chem. Phys., 19, 10087–10110, https://doi.org/10.5194/acp-19-10087-
1071 2019, 2019.

1072 Lucas, R. M., Yazar, S., Young, A. R., Norval, M., de Gruijl F. R., Takizawa, Y., Rhodes, L. E., Sinclair,
1073 C. A., and Neale, R. E.: Human health in relation to exposure to solar ultraviolet radiation under changing
1074 stratospheric ozone and climate, Photochem. Photobiol. Sci., 18, 641, doi: 10.1039/c8pp90060d, 2019.

1075 Madronich, S., McKenzie, R. L., Björn, L. O., and Caldwell, M. M.: Changes in biologically active
1076 ultraviolet radiation reaching the Earth's surface, Journal of Photochemistry and Photobiology B: Biology,
1077 46, 5–19, 1998.

1078 Maksym, T.: Arctic and Antarctic sea ice change: contrasts, commonalities, and causes. Annu. Rev. Mar.
1079 Sci. 11, 187–213, doi:10.1146/annurev-marine-010816-060610, 2019.

1080 (The HadGEM2 Development Team): Martin, G. M., Bellouin, N., Collins, W. J., Culverwell, I. D.,
1081 Halloran, P. R., Hardiman, S. C., Hinton, T. J., Jones, C. D., McDonald, R. E., McLaren, A. J., O'Connor,
1082 F. M., Roberts, M. J., Rodriguez, J. M., Woodward, S., Best, M. J., Brooks, M. E., Brown, A. R., Butchart,
1083 N., Dearden, C., Derbyshire, S. H., Dharssi, I., Doutriaux-Boucher, M., Edwards, J. M., Falloon, P. D.,
1084 Gedney, N., Gray, L. J., Hewitt, H. T., Hobson, M., Huddleston, M. R., Hughes, J., Ineson, S., Ingram, W.
1085 J., James, P. M., Johns, T. C., Johnson, C. E., Jones, A., Jones, C. P., Joshi, M. M., Keen, A. B., Liddicoat,
1086 S., Lock, A. P., Maidens, A. V., Manners, J. C., Milton, S. F., Rae, J. G. L., Ridley, J. K., Sellar, A., Senior,

C. A., Totterdell, I. J., Verhoef, A., Vidale, P. L., and Wiltshire, A.: The HadGEM2 family of Met Office Unified Model climate configurations, Geosci. Model Dev., 4, 723–757, https://doi.org/10.5194/gmd-4-723-2011, 2011.

McKenzie, R., Bernhard, G., Liley, B., Disterhoft, P., Rhodes, S., Bais, A., Morgenstern, O., Newman, P., Oman, L., Brogniez, C., et al.: Success of Montreal Protocol Demonstrated by Comparing High Quality UV Measurements with "World Avoided" Calculations from Two Chemistry-Climate Models, Sci. Rep., 9, 12332, 2019.

McKenzie, R. L., Matthews, W. A., and Johnston, P. V.: The relationship between erythemal UV and ozone, derived from spectral irradiance measurements, Geophys. Res. Lett., 18(12), 2269–2272, 1991.

Neale, R. E., Barnes, P. W., Robson,·T. M., Neale,·P. J., Williamson,·C. E., Zepp, R. G., Wilson, S. R., Madronich,·S., Andrady,·A. L., Heikkilä, A. M., Bernhard, G. H., Bais, A. F., Aucamp, P. J., Banaszak, A. T., Bornman, J. F., Bruckman, L. S., Byrne, S. N., Foereid, B., Häder, D.-P., Hollestein, L. M., Hou, W.-C., Hylander, S., Jansen, M. A. K., Klekociuk, A. R., Liley, J. B., Longstreth, J., Lucas, R. M., Martinez-Abaigar, J., McNeill, K., Olsen, C. M., Pandey, K. K., Rhodes, L. E., Robinson, S. A., Rose, K. C., Schikowski, T., Solomon, K. R., Sulzberger, B., Ukpebor, J. E., Wang, Q.-W., Wängberg, S.-Å., White, C. C., Yazar, S., Young, A. R., Young, P. J., Zhu, L., Zhu, M.: Environmental effects of stratospheric ozone depletion, UV radiation, and interactions with climate change: UNEP Environmental Effects Assessment Panel, Update 2020, Photochemical & Photobiological Sciences, 20, 1–67, https://doi.org/10.1007/s43630-020-00001-x, 2021.

Nichol, S. E., Pfister, G., Bodeker, G. E., McKenzie, R. L., Wood, S. W., and Bernhard, G.: Moderation of cloud reduction of UV in the Antarctic due to high surface albedo, J. Applied Meteorology, 42, 1174–1183, 2003.

Norris, J. R., Allen, R. J., Evan, A. T., Zelinka, M. D., O'Dell, C. W., and Klein, S. A.: Evidence for climate change in the satellite cloud record, Nature, 536, 72–75, doi: 10.1038/nature18273, 2016.

Parkinson, C. L.: A 40-y record reveals gradual Antarctic sea ice increases followed by decreases at rates far exceeding the rates seen in the Arctic. Proc. Natl Acad. Sci. USA, 116, 14414–14423, doi:10.1073/pnas.1906556116, 2019.

Pisoft, P., Sacha, P., Polvani, L. M., Añel, J. A., de la Torre, L., Eichinger, R., Foelsche, U., Huszar, P., Jacobi, C., Karlicky, J., Kuchar, A., Miksovsky, J., Zak, M., and Rieder, H. E.: Stratospheric contraction caused by increasing greenhouse gases, Environ. Res. Lett., 16, 064038, https://doi.org/10.1088/1748-9326/abfe2b, 2021.

Riihelä, A., Bright, R. M., and Anttila, K.: Recent strengthening of snow and ice albedo feedback driven by Antarctic sea-ice loss, Nat. Geosci., 14, 832–836, doi:10.1038/s41561-021-00841-x, 2021.

Sander, R., Jöckel, P., Kirner, O., Kunert, A. T., Landgraf, J., and Pozzer, A.: The photolysis module JVAL-14, compatible with the MESSy standard, and the JVal PreProcessor (JVPP), Geosci. Model Dev., 7, 2653–2662, 2014.

Santer B. D., Wehner, M. F., Wigley, T. M. L., Sausen, R., Meehl, G. A., Taylor, K. E., Ammann., C., Arblaster, J., Washington, W. M., Boyle, J. S., and Brüggemann, W.: Contributions of Anthropogenic and Natural Forcing to Recent Tropopause Height Changes, Science, Vol 301, Issue 5632, 479–483, doi:10.1126/science.1084123, 2003.

Schneider, T., Kaul, C. M., and Pressel, K. G.: Possible climate transitions from breakup of stratocumulus decks under greenhouse warming, Nature Geoscience, 12, 163–167, https://doi.org/10.1038/s41561-019-0310-1, 2019.

Setlow, R. B.: The Wavelengths in Sunlight Effective in Producing Skin Cancer: A Theoretical Analysis, Proc. Nat. Acad. Sci. USA, 71(9), 3363–3366, https://doi.org/10.1073/pnas.71.9.3363, 1974.

Solomon, S., Ivy, D. J., Kinnison, J., Mills, M. J., Neely, R. R., and Schmidt, A.: Emergence of healing in the Antarctic ozone layer, Science 353, 269–274. https://doi.org/10.1126/science.aae0061, 2016.

Stocker, T. F., Qin, D., Plattner, G. K., Tignor, M. M. B., Allen, S. K., Boschung, J., Nauels, A., Xia, Y., Bex, V., and Midgley, P. M.: Climate change 2013 the physical science basis: Working Group I contribution to the fifth assessment report of the intergovernmental panel on climate change vol 9781107057999, 2013.

von der Gathen, P., Kivi, R., Wohltmann, I., Salawitch, R. J., and Rex, M.: Climate change favours large seasonal loss of Arctic ozone, Nature Communications, 12, 3886, https://doi.org/10.1038/s41467-021-24089-6, 2021.

von Storch, H. and Zwiers, F. W.: Statistical analysis in climate research, Cambridge University Press, Cambridge, 1999, ISBN 0 521 45071 3, 484 pp.

Weatherhead, B., Tanskanen, A., Stevermer, A. (Lead Authors), Andersen, S. B., Arola, A., Austin, J., Bernhard, G., Browman, H., Fioletov, V., Grewe, V., Herman, J., Josefsson, W., Kylling, A., Kyrö, E., Lindfors, A., Shindell, D., Taalas, P., and Tarasick, D.: Ozone and ultraviolet radiation, In Arctic Climate Impact Assessment (ACIA), (Chapter 5, pp. 151–182), Cambridge University Press, 2005, Retrieved from https://acia.amap.no/ (last access: 4 September 2022).

Weber, M., Coldewey-Weber, M., Coldewey-Egbers, M., Fioletov, V. E., Frith, S. M., Wild, J. D., Burrows, J. P., Long, C. S., Loyola, D.: Total ozone trends from 1979 to 2016 derived from five merged observational datasets – the emergence into ozone recovery, Atmos. Chem. Phys., 18, 2097–2117, https://doi.org/10.5194/acp-18-2097-2018, 2018.

Weihs, P., Simic, S., Laube, W., Mikielewicz, W., Rengarajan, G., and Mandl, M.: Albedo Influences on Surface UV Irradiance at the Sonnblick High-Mountain Observatory (3106-m Altitude), J. Applied

1154 Meteorology, 38, 1599–1610, https://doi.org/10.1175/1520-0450(1999)038<1599:AIOSUI>2.0.CO;2,
1155 1999.

1156 Wild, M., Gilgen, H., Roesch, A., Ohmura, A., Long, C. N., Dutton, E. G., Forgan, B., Kallis, A., Russak,
1157 V., and Tsvetkov, A.: From dimming to brightening: decadal changes in solar radiation at Earth's surface,
1158 Science, Vol. 308, Issue 5723, 847–850, doi: 10.1126/science.1103215, 2005.

1159 Zerefos, C., Kapsomenakis, J., Eleftheratos, K., Tourpali, K., Petropavlovskikh, I., Hubert, D., Godin-
1160 Beekmann, S., Steinbrecht, W., Frith, S., Sofieva, V., et al.: Representativeness of single lidar stations for
1161 zonally averaged ozone profiles, their trends and attribution to proxies, Atmos. Chem. Phys., 18, 6427–
1162 6440, 2018.

1163 Zerefos, C., Meleti, C., Balis, D., Tourpali, K., Bais, A. F.: Quasi-biennial and longer-term changes in clear
1164 sky UV-B solar irradiance, Geophys. Res. Lett., Vol. 25, No. 23, 4345-4348, 1998.

1165 Zerefos, C. S., Tourpali, K., Zanis, P., Eleftheratos, K., Repapis, C., Goodman, A., Wuebbles, D., Isaksen,
1166 I. S. A., and Luterbacher, J.: Evidence for an earlier greenhouse cooling effect in the stratosphere before
1167 1980 over the Northern Hemisphere, Atmospheric Chemistry and Physics, 14, 7705–7720, doi:
1168 10.5194/acp-14-7705-2014, 2014.

1169 Zhang, R., Wang, H., Fu, Q., Rasch, P. J., and Wang, X.: Unraveling driving forces explaining significant
1170 reduction in satellite-inferred Arctic surface albedo since the 1980s, Proc. Natl. Acad. Sci. USA, 116(48),
1171 23947–23953, doi:10.1073/pnas.1915258116, 2019.

1172

1173

1174 **Table 1.** Ground-based stations with long-term UV measurements used for the evaluation of EMAC CCM

1175 DNA active irradiance simulations. Stations are listed from northern to southern high latitudes and are

1176 grouped as follows: 3 stations at latitudes greater than 55° N, 13 stations between 50° N – 50° S and 4

1177 stations at latitudes greater than 55° S.

Station name	Latitude	Longitude	Period
1. Summit, Greenland*	72.58	-38.45	08/2004-08/2017
2. Barrow, AK, United States*	71.32	-156.68	02/1991-07/2016
3. Sodankylä, Finland	67.37	26.63	01/1990-12/2021
4. Villeneuve d'Ascq, France*	50.61	3.14	01/2000-12/2019
5. Groß-Enzersdorf, Austria*	48.20	16.56	05/1998-11/2019
6. Zugspitze, Germany*	47.42	10.98	08/1995-06/2007
7. Hoher Sonnblick, Austria*	47.05	12.95	01/1997-06/2020
8. Aosta, Italy	45.74	7.36	08/2006-09/2020
9. Observatoire de Haute Provence, France*	43.94	5.70	01/2009-11/2018
10. Thessaloniki, Greece	40.63	22.95	08/1993-12/2019
11. Boulder, CO, United States*	39.99	-105.26	01/2004-12/2019
12. Athens, Greece	37.99	23.78	07/2004-12/2020
13. Mauna Loa, HI, United States*	19.53	-155.58	07/1995-12/2019
14. Reunion Island, St. Denis, France*	-20.90	55.50	03/2009-12/2019
15. Alice Springs, Australia*	-23.80	133.87	01/2005-12/2019
16. Lauder, New Zealand*	-45.04	169.68	01/1991-12/2019
17. Ushuaia, Argentina*	-54.82	-68.32	01/1990-11/2008
18. Palmer, Antarctica*	-64.77	-64.05	03/1990-05/2021
19. Arrival Heights, Antarctica*	-77.83	166.67	01/1990-04/2021
20. South Pole, Antarctica*	-90	0	11/1990-03/2021

1178 *NDACC sites

1179

1180

1181 **Table 2. (a)** Correlation results between model simulations (HIS-SD) and ground-based DNA active
1182 irradiance data for the northern high latitude stations (>55° N), the southern high latitude stations (>55° S),
1183 and the stations between 50° N – 50° S. **(b)** Same as (a) but for the HIS-SD simulation and satellite SBUV
1184 (v8.7) total ozone data. **(c)** Same as (a) but for the HIS-SD simulation and satellite MODIS/Terra cloud
1185 fraction data. Error, t-value, and p-value refer to slope; t-value should be higher than 2.576 for 99%
1186 statistical significance.

1187

(a) DNA active irradiance							
	R	Slope	Error	t-value	p-value	N	RMSE
>55° N	+0.504	0.807	0.125	6.447	<0.0001	124	11.527
>55° S	+0.746	0.879	0.070	12.629	<0.0001	129	14.766
50° N – 50° S	+0.499	0.387	0.045	8.564	<0.0001	223	4.215
(b) Total ozone							
	R	Slope	Error	t-value	p-value	N	RMSE
>55° N	+0.899	0.858	0.037	23.264	<0.0001	131	1.308
>55° S	+0.892	0.888	0.040	22.211	<0.0001	129	3.414
50° N – 50° S	+0.894	0.817	0.028	29.672	<0.0001	223	0.872
(c) Cloud cover							
	R	Slope	Error	t-value	p-value	N	RMSE
>55° N	+0.453	0.362	0.063	5.775	<0.0001	131	4.483
>55° S	+0.485	0.806	0.129	6.230	<0.0001	128	5.003
50° N – 50° S	+0.703	0.721	0.049	14.674	<0.0001	222	5.162

1188

1189

1190

1191

Table 3. Trends (% per decade) in total ozone, DNA active irradiance, and cloudiness from the two model

simulations and the differences between them, i.e., free-running simulation with increasing GHGs (REF)

minus the simulation with fixed GHGs at 1960 levels (FIX), averaged at 3 stations in the northern high

latitudes (>55º N), 4 stations in the southern high latitudes (>55º S), and 13 stations between 50º N – 50º S.

The trends are estimated from the annual mean anomalies shown in Figures 4, 5, 6.

1197

table									
>55º N (3 stations)									
Trends (% per decade)	**REF**			**FIX**			**Difference**		
	1960-1999	**2000-2049**	**2050-2099**	**1960-1999**	**2000-2049**	**2050-2099**	**1960-1999**	**2000-2049**	**2050-2099**
Ozone	−0.55 ± 0.21	0.50 ± 0.16	0.41 ± 0.17	−1.35 ± 0.26	0.36 ± 0.15	0.05 ± 0.15	0.79 ± 0.24	0.14 ± 0.16	0.36 ± 0.17
DNA active irradiance	1.03 ± 0.77	−1.75 ± 0.56	−2.47 ± 0.60	2.61 ± 0.78	−1.15 ± 0.46	−0.83 ± 0.57	−1.57 ± 0.96	−0.59 ± 0.68	−1.64 ± 0.76
Clouds	−0.21 ± 0.30	−0.10 ± 0.23	0.32 ± 0.20	−0.20 ± 0.43	0.02 ± 0.25	0.19 ± 0.27	−0.29 ± 0.45	−0.39 ± 0.25	0.29 ± 0.27
>55º S (4 stations)									
Trends (% per decade)	**REF**			**FIX**			**Difference**		
	1960-1999	**2000-2049**	**2050-2099**	**1960-1999**	**2000-2049**	**2050-2099**	**1960-1999**	**2000-2049**	**2050-2099**
Ozone	−3.78 ± 0.57	2.63 ± 0.31	1.42 ± 0.29	−4.65 ± 0.48	2.28 ± 0.41	0.58 ± 0.31	0.87 ± 0.56	0.35 ± 0.46	0.84 ± 0.42
DNA active irradiance	5.70 ± 0.97	−4.92 ± 0.55	−1.68 ± 0.43	7.61 ± 0.92	−4.81 ± 0.75	−0.72 ± 0.38	−1.91 ± 0.95	−0.10 ± 0.82	−0.97 ± 0.58
Clouds	−0.36 ± 0.39	−0.71 ± 0.28	−0.28 ± 0.26	0.18 ± 0.31	−0.05 ± 0.22	−0.01 ± 0.26	−0.54 ± 0.47	−0.53 ± 0.35	−0.21 ± 0.35
50º N – 50º S (13 stations)									
Trends (% per decade)	**REF**			**FIX**			**Difference**		
	1960-1999	**2000-2049**	**2050-2099**	**1960-1999**	**2000-2049**	**2050-2099**	**1960-1999**	**2000-2049**	**2050-2099**
Ozone	−0.61 ± 0.14	0.42 ± 0.11	0.02 ± 0.12	−1.27 ± 0.16	0.36 ± 0.10	0.12 ± 0.09	0.66 ± 0.10	0.06 ± 0.08	−0.10 ± 0.09
DNA active irradiance	1.55 ± 0.44	−0.53 ± 0.35	0.86 ± 0.35	1.75 ± 0.48	−0.54 ± 0.32	0.05 ± 0.28	−0.20 ± 0.58	0.01 ± 0.44	0.81 ± 0.39
Clouds	−1.15 ± 0.29	−0.30 ± 0.27	−0.60 ± 0.25	0.16 ± 0.30	−0.25 ± 0.23	−0.16 ± 0.19	−1.21 ± 0.42	−0.12 ± 0.30	−0.50 ± 0.27

1198

1199

1200

1201 **Table 4.** Same as Table 3 but for the winter months, January (J), February (F), and March (M) for the

1202 northern high latitude stations. Due to the polar night, UV results for January and February are not shown

1203 due to large standard errors.

1204

>55º N (3 stations)									
Trends (% per decade)	**REF**			**FIX**			**Difference**		
	1960-1999	**2000-2049**	**2050-2099**	**1960-1999**	**2000-2049**	**2050-2099**	**1960-1999**	**2000-2049**	**2050-2099**
Ozone (J)	−1.66 ± 0.74	1.81 ± 0.53	0.49 ± 0.53	−1.32 ± 0.72	0.28 ± 0.50	0.28 ± 0.54	−0.34 ± 1.09	1.53 ± 0.64	0.21 ± 0.73
Ozone (F)	−2.27 ± 0.74	2.00 ± 0.59	0.88 ± 0.58	−1.65 ± 0.83	0.21 ± 0.54	0.31 ± 0.44	−0.62 ± 0.96	1.79 ± 0.78	0.58 ± 0.71
Ozone (M)	−2.98 ± 0.53	0.75 ± 0.50	0.66 ± 0.35	−3.04 ± 0.71	0.58 ± 0.39	−0.54 ± 0.41	0.06 ± 0.83	0.17 ± 0.58	1.20 ± 0.51
DNA active irradiance (J)	Polar night	Polar night	Polar night	Polar night	Polar night	Polar night	Polar night	Polar night	Polar night
DNA active irradiance (F)	Polar night	Polar night	Polar night	Polar night	Polar night	Polar night	Polar night	Polar night	Polar night
DNA active irradiance (M)	3.03 ± 1.97	−0.63 ± 1.52	−2.83 ± 1.22	7.20 ± 1.77	−0.09 ± 1.44	−0.98 ± 1.27	−3.28 ± 2.55	−0.06 ± 2.18	−1.90 ± 1.51
Clouds (J)	−0.67 ± 0.61	1.29 ± 0.63	0.94 ± 0.48	1.11 ± 0.77	0.03 ± 0.53	0.52 ± 0.49	−1.77 ± 0.92	1.25 ± 0.88	0.39 ± 0.68
Clouds (F)	−0.07 ± 0.86	0.60 ± 0.68	1.30 ± 0.57	0.55 ± 0.81	−0.14 ± 0.66	0.06 ± 0.58	−0.62 ± 1.11	0.74 ± 0.93	1.24 ± 0.82
Clouds (M)	0.35 ± 0.70	1.15 ± 0.60	1.33 ± 0.61	0.23 ± 1.02	0.21 ± 0.69	−0.17 ± 0.64	0.12 ± 1.12	0.94 ± 0.88	1.49 ± 0.79

1205

1206

1207

1208   **Table 5.** Statistical test results for the difference between two trends in DNA active irradiance (trend of
1209   1960-2049 minus trend of 2050-2099), for the northern high latitude stations (>55° N), the southern high
1210   latitude stations (>55° S), and the stations between 50° N – 50° S.

1211

Latitudes	>55° N (3 stations)		>55° S (4 stations)		50° N – 50° S (13 stations)	
	1960–2049	2050–2099	1960–2049	2050–2099	1960–2049	2050–2099
N	553	315	630	350	1080	600
slope, $b/year$ (Eq. 4)	–0.173	–0.186	–0.116	–0.096	–0.033	0.081
s_b (Eqs. 5 and 6)	0.027	0.062	0.026	0.048	0.015	0.037
$s_{(b_1-b_2)}$ (Eq. 3)	0.068		0.054		0.040	
$t-value$ (Eq. 3)	0.185		–0.376		–2.844	
degrees of freedom	864		976		1676	
significance level	0.05		0.05		0.05	
$p-value$	0.853		0.707		0.005	
$t-critical$	1.96		1.96		1.96	
Significantly different trends	No		No		Yes	

1212

1213

1214

1215 **Table 6. (a)** Coefficients of multiple regression analysis according to Eq. (7), applied to the differences

1216 between the two model simulations, REF and FIX, for the period 2050–2099, for the northern high latitude

1217 stations (>55º N), the southern high latitude stations (>55º S), and the stations between 50º N – 50º S. **(b)**

1218 Trends (% per decade) for the period 2050-2099 in the DNA active irradiance, the ozone-related DNA

1219 active irradiance component and the cloud-related DNA active irradiance component.

1220

(a) MLR coefficients (2050–2099)			
	>55º N (3 stations)	>55º S (4 stations)	50º N – 50º S (13 stations)
$a \pm error$	−4.473 ± 0.976	−1.994 ± 0.670	−0.557 ± 0.336
$\beta_{O_3} \pm error$	−2.017 ± 0.220	−0.667 ± 0.071	−2.831 ± 0.128
$\beta_{cloud} \pm error$	−0.749 ± 0.090	−0.367 ± 0.065	−0.642 ± 0.035

(b) Trends (% per decade) (2050–2099)			
	>55º N (3 stations)	>55º S (4 stations)	50º N – 50º S (13 stations)
DNA active irradiance	−1.86 ± 0.61%	−0.96 ± 0.48%	0.81 ± 0.37%
Ozone-related DNA active irradiance component	−0.72 ± 0.25%	−0.57 ± 0.21%	0.27 ± 0.20%
Cloud-related DNA active irradiance component	−0.21 ± 0.24%	0.07 ± 0.13%	0.33 ± 0.17%

1221

1222

1223

1224   **Table 7.** Trends and their standard errors (% per decade) in the differences between the two model

1225   simulations, REF and FIX, for the DNA active irradiance, total ozone, cloud cover and surface albedo at

1226   Barrow (Alaska) and Palmer (Antarctica) for the periods 1960–1999, 2000–2049 and 2050–2099.

1227

Trends (% per decade)	Barrow, Alaska			Palmer, Antarctica		
	1960-1999	**2000-2049**	**2050-2099**	**1960-1999**	**2000-2049**	**2050-2099**
DNA active irradiance	−2.88 ± 1.67	−2.18 ± 1.17	−2.14 ± 1.12	0.75 ± 1.47	−1.79 ± 1.08	−0.33 ± 0.90
Ozone	0.39 ± 0.24	0.06 ± 0.17	0.44 ± 0.19	−0.02 ± 0.54	0.23 ± 0.37	0.54 ± 0.40
Clouds	−0.96 ± 0.78	0.42 ± 0.54	0.60 ± 0.52	−1.60 ± 0.65	0.41 ± 0.49	−0.46 ± 0.48
Surface albedo	0.88 ± 1.33	−6.42 ± 0.80	−2.73 ± 0.89	0.08 ± 0.82	−1.52 ± 0.51	−1.60 ± 0.53

1228

1229

1230

1231
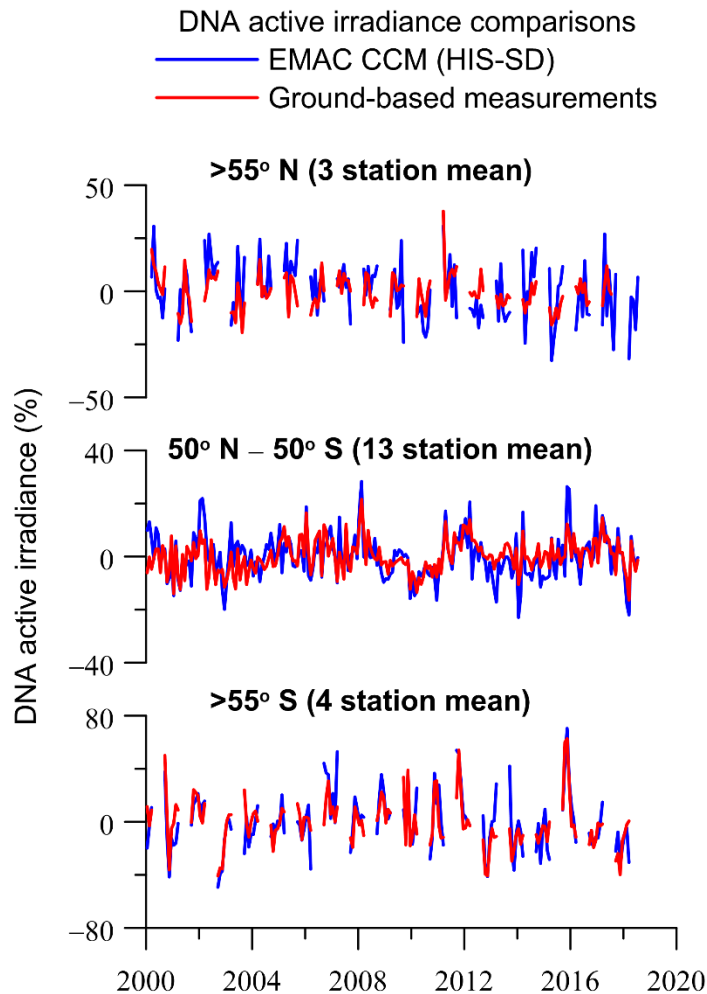
1232

1233

1234 **Figure 1.** Comparison of model simulations of DNA active irradiance with averages of ground-based
1235 measurements at 3 UV stations in the northern high latitudes (>55º N) (upper panel), 13 UV stations from
1236 50º N to 50º S (middle panel) and 4 UV stations in the southern high latitudes (>55º S) (lower panel). The
1237 y-axis shows monthly de-seasonalized DNA active irradiance data (in %). The monthly data at each station
1238 were de-seasonalized by subtracting the long-term monthly mean (2000–2018) pertaining to the same
1239 calendar month and were expressed in %. Then, the average over each geographical zone was estimated by
1240 averaging the de-seasonalized data of the stations belonging to each geographical zone. Shown are data
1241 from March to September for the northern high latitudes and from September to March for the southern
1242 high latitudes.

1243

1244

1245
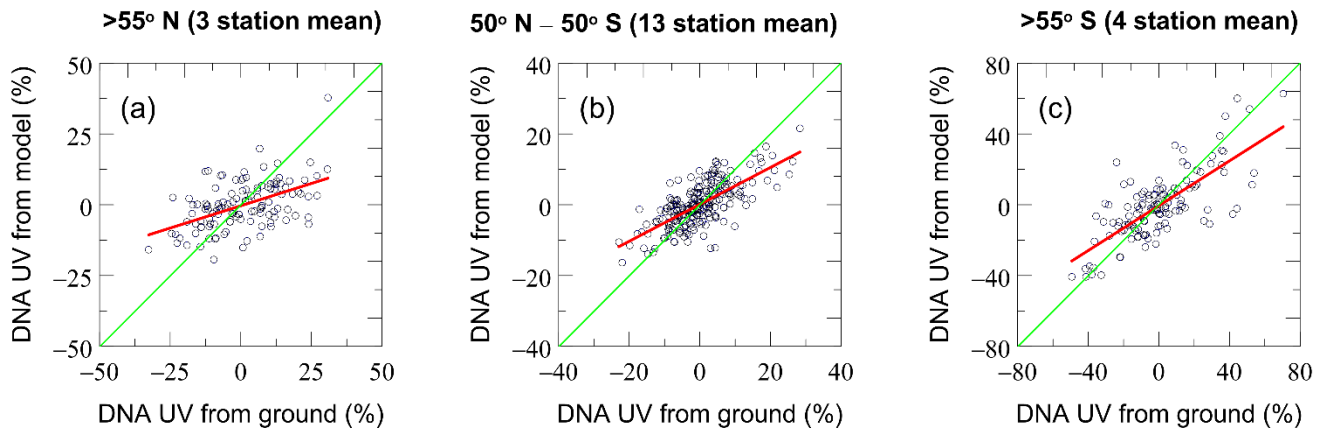
1246 **Figure 2.** Scatter plots of DNA active irradiance from simulated and ground-based data shown in Figure 1
1247 for **(a)** 3 UV stations in the northern high latitudes (>55º N), **(b)** 13 UV stations from 50º N to 50º S and **(c)**
1248 4 UV stations in the southern high latitudes (>55º S).

1249

1250

1251

1252
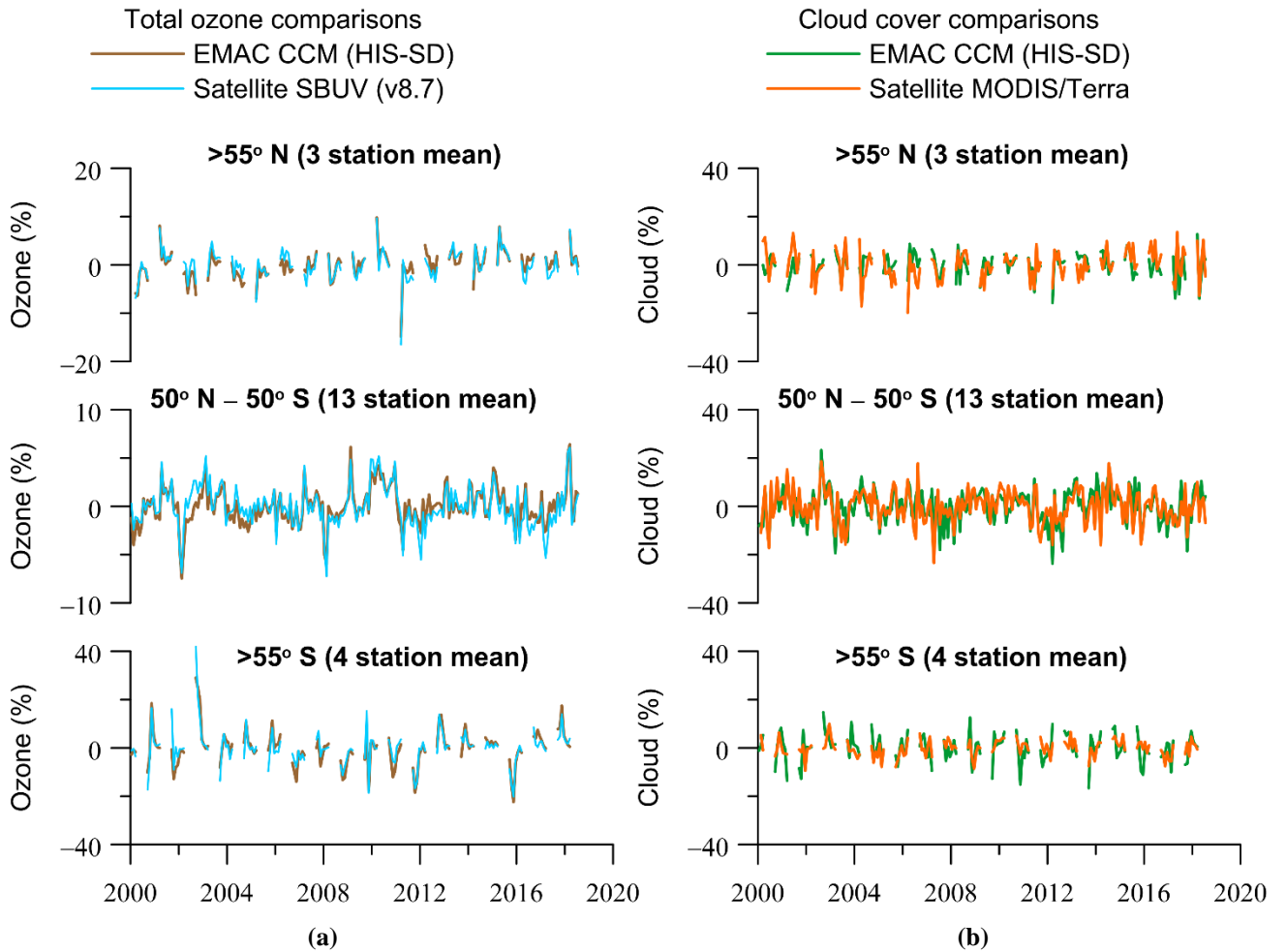
Figure 3. **(a)** Same as in Figure 1 but for ozone column. **(b)** For cloud cover. The y-axes show monthly de-
seasonalized anomalies (in %) relative to the long-term monthly mean (2000–2018). Shown are monthly
anomalies from March to September for the northern high latitudes, and from September to March for the
southern high latitudes. For 50° N–50° S, we present all months.

1258

1259
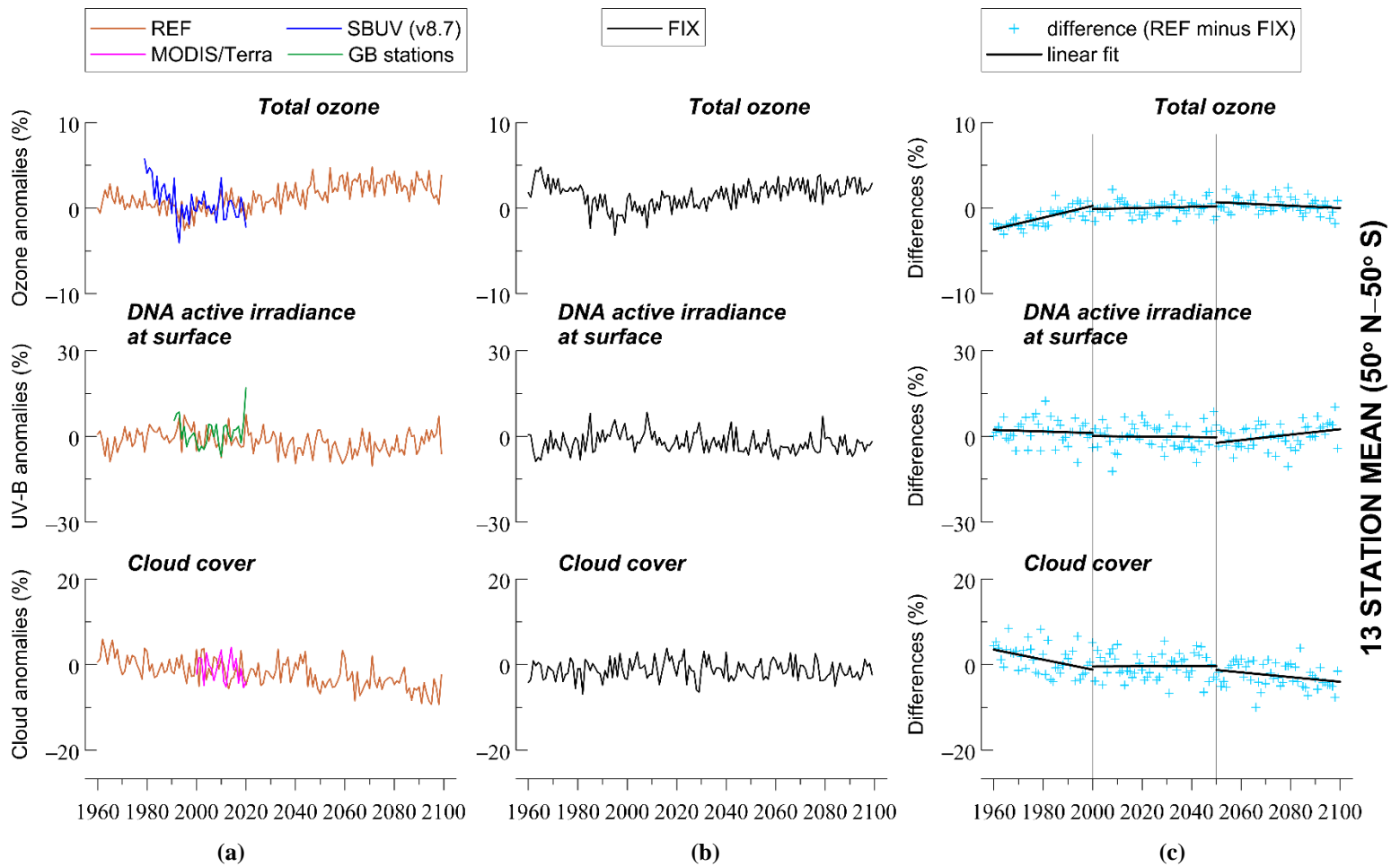
Figure 4. Changes in total ozone, DNA active irradiance and cloud cover averaged at 13 UV stations from 50º N to 50º S, based on simulations with increasing and fixed GHGs mixing ratios. **(a)** REF is the simulation with increasing GHGs according to RCP-6.0. **(b)** FIX is the simulation with fixed GHGs emissions at 1960 levels. **(c)** Difference between the two model simulations, indicating the impact of increasing GHGs. The y-axes in (a) and (b) show yearly averaged data (in %) calculated from de-seasonalized monthly data. The monthly data were de-seasonalized relative to the long-term monthly mean (1990–2019) and were expressed in %. For stations between 50º N–50º S we used all months to calculate the annual average.

1268
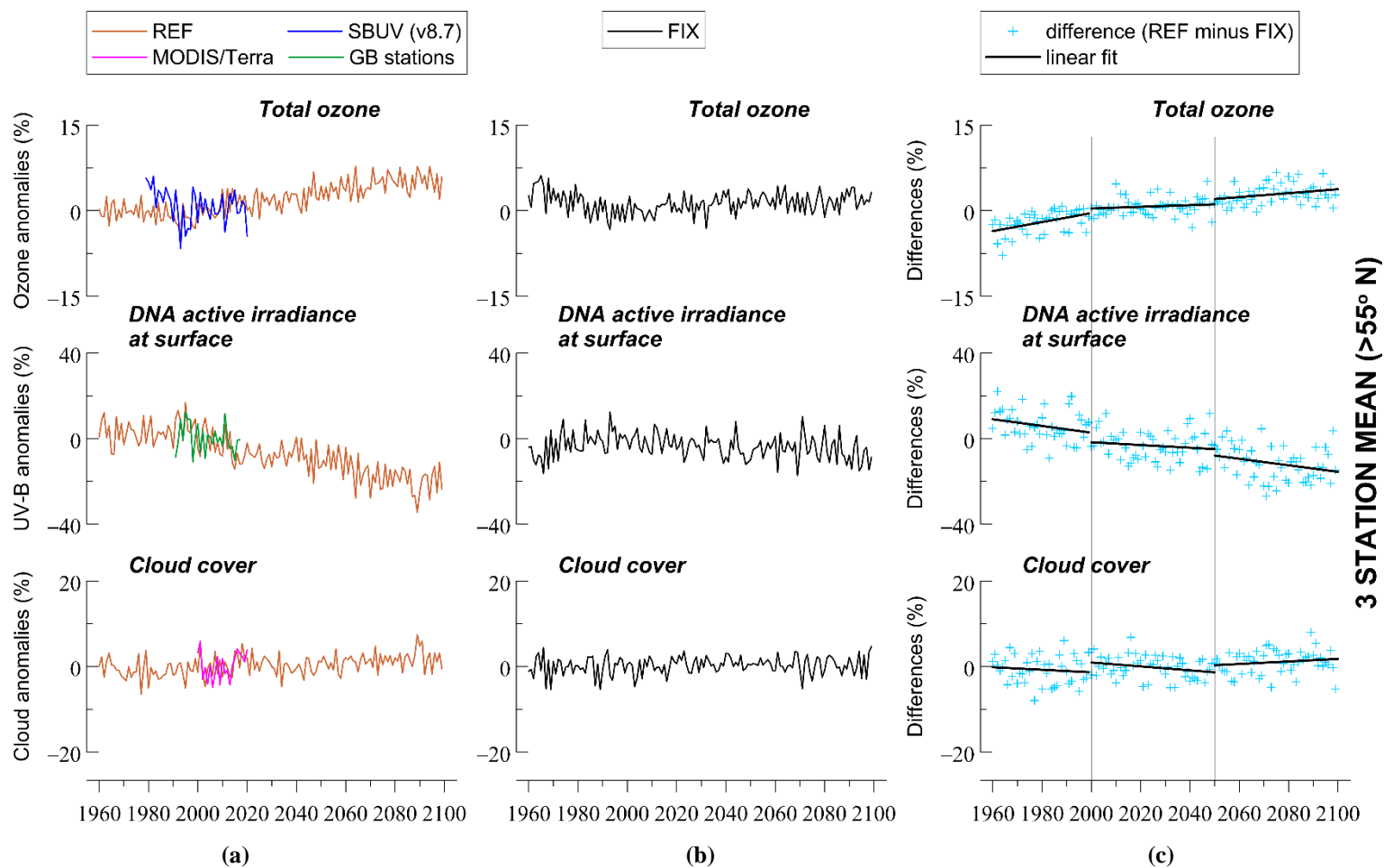
1269

1270   **Figure 5.** Same as Figure 4 but for 3 UV stations in the northern high latitudes (>55° N). The y-axes in (a)

1271   and (b) show averages of monthly de-seasonalized anomalies from March to September.

1272

1273
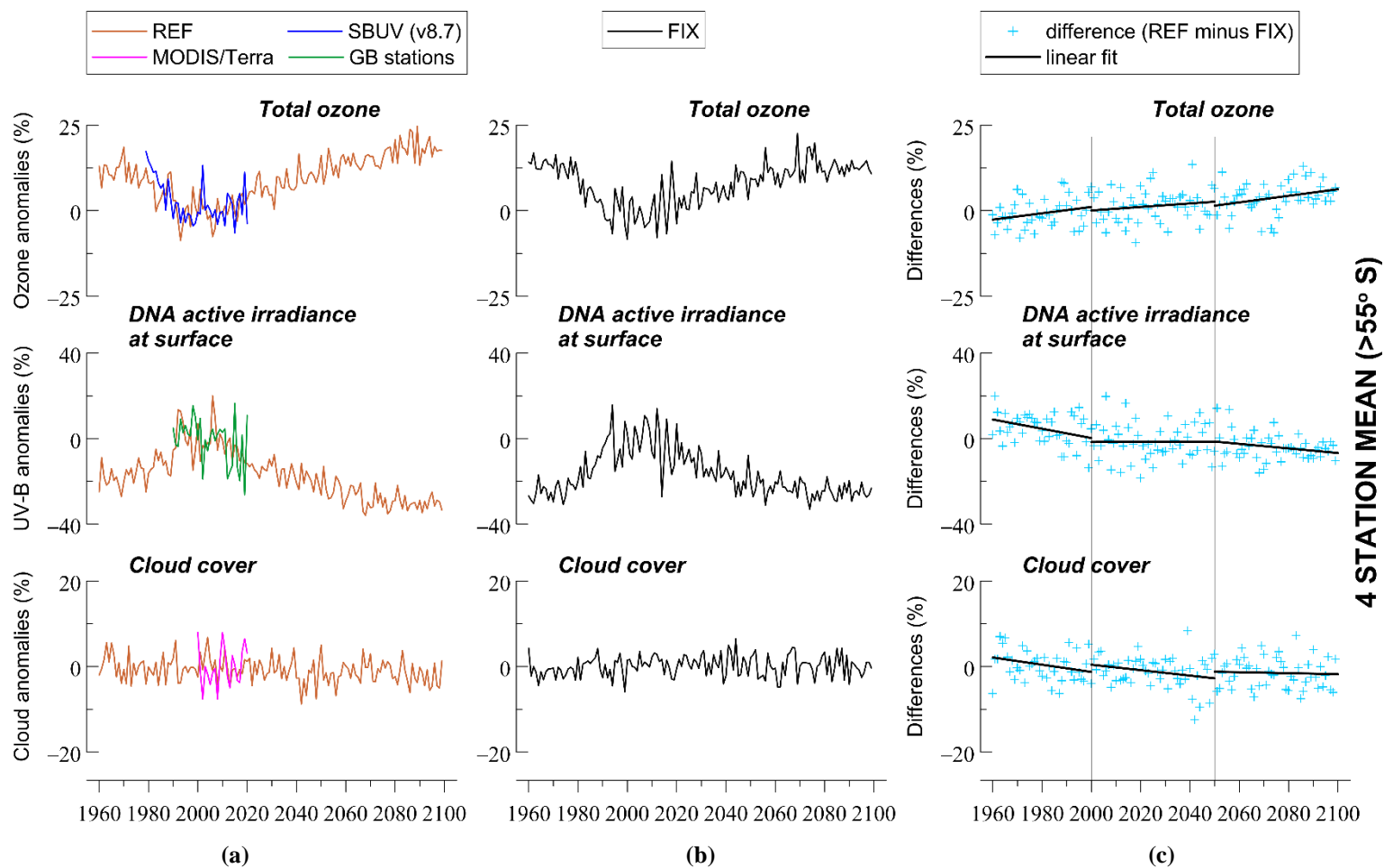
Figure 6. Same as Figure 4 but for 4 UV stations in the southern high latitudes (>55° S). The y-axes in (a)

and (b) show averages of monthly de-seasonalized anomalies from September to March.

1274

1275

1276

1277

1278
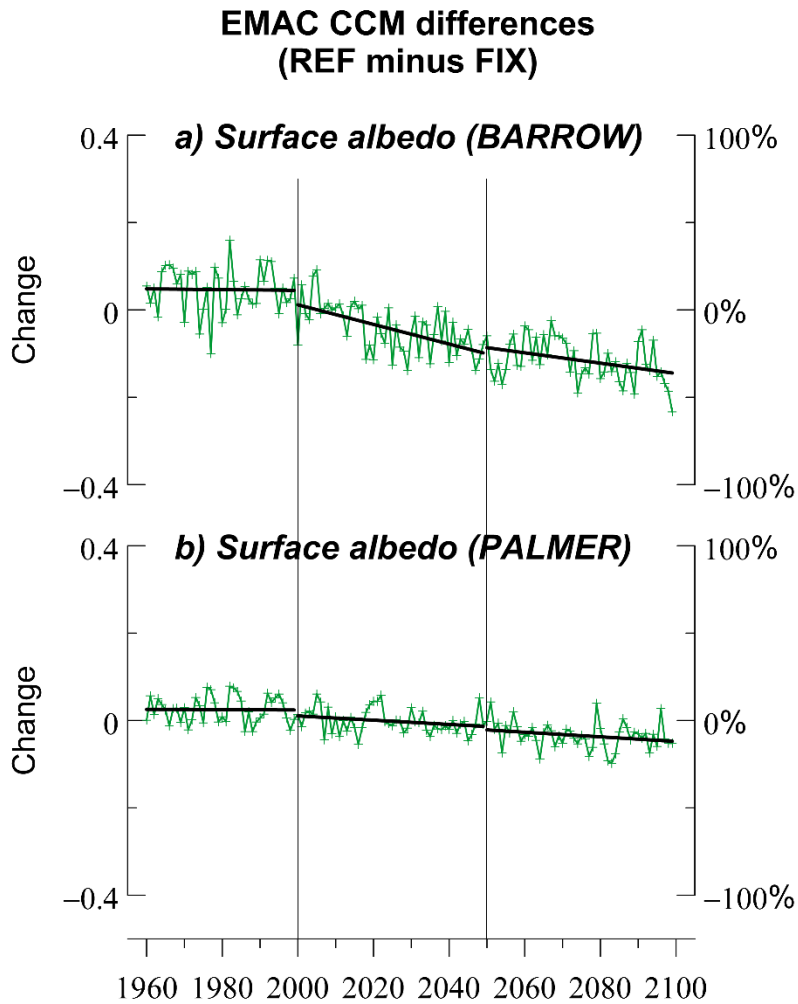
Figure 7. **(a)** Changes in surface albedo at Barrow, Alaska, and **(b)** at Palmer, Antarctica, derived from the differences between the two model simulations: the one with increasing GHGs (REF) and the one with fixed GHGs (FIX). Results refer to the summer season. Data were de-seasonalized with respect the period 1990–2019 and then were averaged from March to September at Barrow, and from September to March at Palmer. The left y-axis shows the differences in surface albedo values and the right y-axis shows the respective differences in % of the mean.

1285

1286